Charge-Carrier Dynamics and Relaxation in Cs_2SnI_6 Perovskite for Energy Storage: Existence of Anharmonic Rattling-Assisted Polaron Dynamics

Moumita Ghosh,[1,§] Pulak Pal,[1,§] Tufan Paul,[2] Soumen Maiti,[3] Souvik Bhattacharjee,[1] Kausik Sardar,[2] Aditi Sahoo,[4] Aswini Ghosh,[5,*] and Kalyan Kumar Chattopadhyay[1,2,†,‡]

[1] *Departments of Physics, Jadavpur University, Kolkata 700032, India*

[2] *School of Materials Science and Nanotechnology, Jadavpur University, Kolkata 700032, India*

[3] *Department of Physics, St. Thomas College of Engineering & Technology, Kolkata 700023, India*

[4] *Advanced Mechanical and Materials Characterization Division, CSIR-Central Glass & Ceramic Research Institute, Kolkata 700032, India*

[5] *School of Physical Sciences, Indian Association for the Cultivation of Science, Jadavpur, Kolkata 700032, India*

(Received 27 February 2023; revised 27 September 2023; accepted 16 October 2023; published 15 November 2023)

We have explored different aspects of charge-carrier dynamics and relaxation in lead-free Cs_2SnI_6 double perovskite using dielectric spectroscopy and assessed its electrochemical response. The cubic phase ($Fm\bar{3}m$) with a lattice constant of 11.644 Å is confirmed for synthesized perovskite. The phonon dispersion illustrated by density-functional theory indicates the existence of soft optical modes triggered by anharmonic rattling of Cs atoms and dynamical rotation of SnI_6 octahedra. Complex impedance spectra have provided details of the contributions of grain boundaries, grains, and anharmonic rattling to charge-carrier dynamics. The Cs_2SnI_6 exhibits electrical conductivity of 3.77×10^{-5} S cm^{-1} at ambient conditions. The values of the power-law exponent for all temperatures suggest superlinear power-law (SPL) behavior of the ac conductivity. The relaxation time and the stretched exponent in the Kohlrausch-Williams-Watts (KWW) function of the electric modulus are caused by charge-carrier short-range mobility and the hopping of rattling-assisted polarons. The supercapacitor fabricated with Cs_2SnI_6 as the electrode has delivered a specific capacitance of 3830 F g^{-1} at a current density of 2 A g^{-1}. A quasi-solid-state asymmetric supercapacitor device was also fabricated, which delivered an energy density of 51 Wh kg^{-1} and a power density as high as 852 W kg^{-1} at a current density of 1 A g^{-1}. We believe this work will open up the avenue to another generation of lead-free, perovskite-based, sustainable energy-storage systems.

DOI: 10.1103/PhysRevApplied.20.054032

I. INTRODUCTION

Along with the widespread progress of hybrid perovskite solar cells [1–3] in the last decade, metal halide perovskites (MHPs) embraced a wide range of applicability in energy-harvesting and storage devices, including photodetectors [4,5], light-emitting diodes [6], memory devices [7–9], and nanogenerators [10–12]. This wide range of applications is attributed to their various properties, like superior charge transport, optoelectronic, dielectric, and photovoltaic properties. However, the commercial applications of Pb-based organic perovskite materials are hampered by their (i) poor stability when exposed to heat, light, and moisture [13,14] and (ii) environmental toxicity due to the presence of Pb [15].

The structure of halide perovskite is represented by ABX_3, where "A" is a cation, which can be both organic and inorganic, "B" represents a metal ion, and "X" represents a halogen ion. In an ideal cubic structure, "B" cations are in sixfold coordination, making an octahedral structure and "A" cations are in 12-fold cubo-octahedral coordination. The "A" cations are generally larger in size than the "B" cations. Subsequently, several approaches have been employed in order to replace Pb, including (but not limited to) homovalent and heterovalent substitution. In a homovalent substitution, divalent Pb^{2+} has been replaced by a divalent cation like Sn^{2+} or Ge^{2+} [16–18]. Although Sn^{2+} and Ge^{2+} could be successfully incorporated to substitute Pb, they are prone to oxidation in ambient air. In the heterovalent substitution approach, the divalent Pb^{2+} cation can be replaced either by a trivalent metal cation, like Bi^{3+} or Sb^{3+}, and a monovalent cation like Ag^{+}, which gives rise to a double perovskite structure, or by a combination of two trivalent cations, viz., Bi^{3+}, Sb^{3+}, etc. [19]. Lead-free inorganic perovskites are favorable in terms of

*sspag@iacs.res.in

†kalyank.chattopadhyay@jadavpuruniversity.in

‡kalyan_chattopadhyay@yahoo.com

§These authors contributed equally to this paper.

nontoxicity and stability issues.Cs_2SnI_6 is one of the most widely explored inorganic double perovskites that show excellent stability against oxidation [20,21]. Due to its stability in air, nontoxicity, and other superior properties, such as electrical properties, absorption coefficient, etc., the Cs_2SnI_6 perovskite has emerged as a potential candidate for a wide range of applications, like resistive switching, LEDs, solar cells, nanogenerators, and photodetectors, etc. [22,23]. It is significant to note that the halide perovskites are mixed ionic and electronic conductors. It is also worthy to note that electrons in perovskites form quasiparticles, called polarons, due to their interaction with the lattice deformation present there. The cooperative deformation of $[BX_6]$ octahedra framework in perovskites occurs due to the size mismatch of *A*-site cations and the cubo-octahedral void generated by neighboring *X*-site anions, giving rise to the formation of polarons. Generally, two types of polarons, such as large polarons and small polarons, exist depending on the size (radius) of the polarons. For small polarons, the polaron radius is confined in a single unit cell, while the polaron radius extends over many unit cells for large polarons [24–30].The *n*-type Cs_2SnI_6 perovskite is a vacancy-ordered double perovskite with covalent and ionic bonding [26]. The soft optical modes of a phonon are created by the anharmonic rattling motion of Cs atoms in the channel created by $[SnI_6]^{2-}$ and the dynamic rotation of SnI_6 octahedra [26].

The MHPs demonstrate intriguing charge-transport properties compared to the typical III-V and other conventional inorganic semiconductors. The hysteresis observed in the *J-V* curves (also an indicator of ferroelectricity) reveals critical insights into the ionic transport mechanism in MHPs [31,32]. The low-frequency (approximately 1 Hz) dielectric response of $MAPbX_3$ increases by 3 orders of magnitude when illuminated with photons with energies greater than its band gap [33]. The photoluminescence study in a mixed halide system has shown that the halide ions segregate into iodide- and bromide-rich domains upon photoexcitation [34]. Importantly, even if stationary defects are assumed, these observations cannot be justified by the semiconductor theory and necessitate a thorough investigation of the dielectric properties of such materials. The high ionic conductivity of perovskite materials has led to a variety of technological applications, such as solar cells, Li-ion batteries, dual-ion batteries, photobatteries, supercapacitors, and so on [35–41]. Despite the potential applications of these MHPs, a detailed and fundamental understanding of charge-carrier dynamics and relaxation mechanisms is still lacking. It may be mentioned that the dielectric spectroscopy is an exceptional tool for investigating charge-carrier dynamics, relaxation mechanisms, ionic conductivity, ferroelectric, and piezoelectric features of various materials, including polymer electrolytes, ceramics, transitional metal oxides, and halide perovskites [42–44].

In this present report, we have synthesized the lead-free vacancy-ordered Cs_2SnI_6 double perovskite using hydrothermal process and characterized its structural, optical, and temperature-dependent dielectric properties. The cubic phase with $Fm\bar{3}m$ space group was confirmed from the Rietveld refinement of the observed X-ray diffraction (XRD) profile with a lattice constant of 11.644 Å. To get insights into the charge-carrier dynamics and relaxation mechanism, the dielectric spectroscopic data in a wide temperature ($T = 193$ K–473 K) and frequency range (f = 4 Hz–8 MHz) has been measured and analyzed using different theoretical models. The contribution of the grain boundaries, grains, and rattling-assisted polaron response to the dynamics of charge carriers at different temperatures has been described by the quantitative analysis of dielectric spectra in terms of impedance, ac conductivity and modulus formalisms. A three-electrode supercapacitor was fabricated using Cs_2SnI_6 perovskite at ambient conditions for the storage of energy, and its cyclic voltammetry, galvanometric charge-discharge, and electrochemical impedance studies were performed, providing a promising result. An understanding of storage mechanisms are presented here. The supercapacitor achieves specific discharge capacitances of 3830, 2187, 1363, 1041, 462, and 199 F g^{-1} at different current densities of 2, 4, 6, 8, 10, and 15 A g^{-1}, respectively. A quasi-solid-state asymmetric supercapacitor device, fabricated with the Cs_2SnI_6 perovskite, delivered an energy density of 51 Wh kg^{-1} and a power density of 852 W kg^{-1} corresponding to a current density of 1 A g^{-1}.

II. EXPERIMENTAL DETAILS

A. Synthesis of lead-free Cs_2SnI_6 double perovskite

1 mmol (237 mg) tin acetate [$Sn(CH_3CO_2)_2$, Sigma-Aldrich] and 2 mmol (384 mg) cesium acetate ($C_2H_3O_3Cs$, 99.99%, Sigma-Aldrich) were dissolved in 5-ml hydroiodic acid (HI, Alfa-Aesar). The solution was stirred at room temperature for about 1 h at 700 rpm and was then kept at 150 °C for 2 h in a 25-ml Teflon container. Afterwards, it was left to cool down to room temperature, and was centrifuged three times with iso-propyl alcohol (IPA, Alfa-Aesar), and dried overnight in a vacuum oven. A schematic diagram of the synthesis process of the sample with digital images of synthesis solutions taken at different times during the synthesis process and final product is shown in Fig. S1 within the Supplemental Material [45].

B. Characterizations

X-ray diffraction (XRD), field-emission scanning electron microscopy (FESEM), high-resolution transmission electron microscopy (HRTEM), ultraviolet-visible (UV-vis) spectroscopy, and X-ray photoelectron spectroscopy (XPS) were carried out to characterize the Cs_2SnI_6 perovskite. The dielectric measurements, viz., the

conductance $G(\omega)$ and capacitance $C(\omega)$ of Cs_2SnI_6 halide perovskite, were carried out at different temperatures using an LCR meter (HIOKI, model: IM 3536) in the frequency range of 4 Hz–8 MHz with a perturbation potential of 1.0 V. The details of this material characterization have been provided within the Supplemental Material [45].

C. Computational details for DFT calculations

All first principles calculations on Cs_2SnI_6 were performed with the CASTEP (CAmbridge Serial Total Energy Package), which is based on density-functional theory (DFT) [46,47]. Norm-conserving plane-wave pseudopotentials were employed to describe the electron-ion interactions [48]. The Perdew-Burke-Ernzerhof (PBE) functional under the generalized gradient approximation (GGA) [49] and accompanying Koeling-Harmon relativistic treatment [47] delineated the exchange-correlation energy between electrons [50]. Both the shape and volume of the initial unit cell were optimized including the relaxation of all atomic positions. The respective convergence threshold, maximum displacement, and maximum force in this calculation were taken as 5.0×10^{-6} eV/atom, 5.0×10^{-4} Å and 0.01 eV/Å, respectively. The electronic bandstructure, electronic density of states (DOS), phonon dispersion, density of phonon states, optical properties, thermodynamic, and other electronic properties were calculated against a $4 \times 4 \times 4$ k-point mesh, where the cutoff energy was limited to 440 eV. Group theoretical calculations were performed using the VIBRATE! software for the structure. The details are presented within the Supplemental Material [45].

D. Electrochemical characterization of the perovskite in the three-electrode supercapacitor

The working electrode to investigate the electrochemical energy-storage behavior of the Cs_2SnI_6 perovskite in a supercapacitor was prepared using the Cs_2SnI_6 perovskite, carbon black (CB), and polyvinylidene fluoride (PVDF) as the binder with a weight ratio of 8:1:1. Initially, a mixture of Cs_2SnI_6, PVDF and CB in the above ratio was added to 300 µl of NMP to obtain a homogeneous slurry paste. The Ni foam (NF) was washed with hydrochloric acid (HCl), acetone, and deionized (DI) water separately and dried in a vacuum oven. Subsequently, the slurry paste was pressed over the Ni foam with active area (1.0×0.5 cm^2) and dried overnight at 80 °C in the oven. The weight of the active material coated in the electrode is about 5.4 mg.

Electrochemical performance was executed in a 1-M KOH aqueous solution at room temperature using PGSTAT 302N Autolab. A platinum wire and Ag/AgCl were used as the counter electrode and reference, respectively. All electrochemical measurements, namely cyclic voltammetry (CV), galvanostatic charge-discharge (GCD), and electrochemical impedance spectroscopy (EIS) were carried out to predict the energy-storage performance of the synthesized perovskite.

E. Fabrication of supercapacitor device and electrochemical measurements

For asymmetric supercapacitor device fabrication, activated carbon (AC) (Sigma Aldrich) was used as an active material. The AC electrode was prepared by coating a NMP-based slurry containing AC powder, acetylene carbon black, and PVDF in the ratio of 80:10:10 (wt %) onto 1 cm × 1 cm Ni foam. After coating of the slurry on the Ni foam, the electrodes were dried at 90 °C under vacuum for 1 day. Similarly, another electrode was prepared by coating NMP-based slurry of Cs_2SnI_6 perovskite, acetylene carbon black, and PVDF in the ratio of 70:15:15 (wt %) onto 1 cm × 1 cm Ni foam. The active mass loadings in the device electrodes were 5.45 mg for the perovskite electrode and 7.23 mg for the AC electrode. The poly(vinyl alcohol) (PVA), KOH, and deionized (DI) water were used for the preparation of the gel polymer electrolyte. A mixture of PVA, KOH, and DI water was stirred vigorously at 90 °C until the solution became transparent and homogeneous. It was cooled to ambient conditions after the gel formation to remove the excess bubbles. Finally, an AC/PVA-KOH gel plus separator/Cs_2SnI_6 perovskite asymmetric supercapacitor device was assembled at ambient conditions. Electrochemical measurements such as CV, charge-discharge, and electrochemical impedance of the asymmetric supercapacitor were performed using a Gamry Interface 1000 (potentiostat/galvanostat/ZRA) system. We used the total active mass of both electrodes for calculating the specific capacitance from CV and GCD in asymmetric device system.

III. RESULTS AND DISCUSSION

A. Structural and morphological characterization of the Cs_2SnI_6 perovskite

XRD analysis was done to verify the purity and crystal structure of the Cs_2SnI_6. The XRD pattern with Rietveld refinement of the synthesized Cs_2SnI_6 using the Fullprof-software is shown in Fig. 1(a). The atomic model of cubic Cs_2SnI_6 obtained from VESTA software is shown in the inset of Fig. 1(a). The XRD profile in Fig. 1(a) reveals the pure phase formation of cubic Cs_2SnI_6 (PDF no. 51-0466). The diffraction peaks at 13.12°, 26.48°, 30.72°, 43.97°, and 46.07° correspond to the (111), (222), (400), (440), and (531) planes of the cubic Cs_2SnI_6 perovskite, which is consistent with the results reported in the literature [51]. The synthesized Cs_2SnI_6 perovskite is in the cubic lattice system with the space group $Fm\bar{3}m$ and a lattice constant of 11.644 Å. The Rietveld refinement also

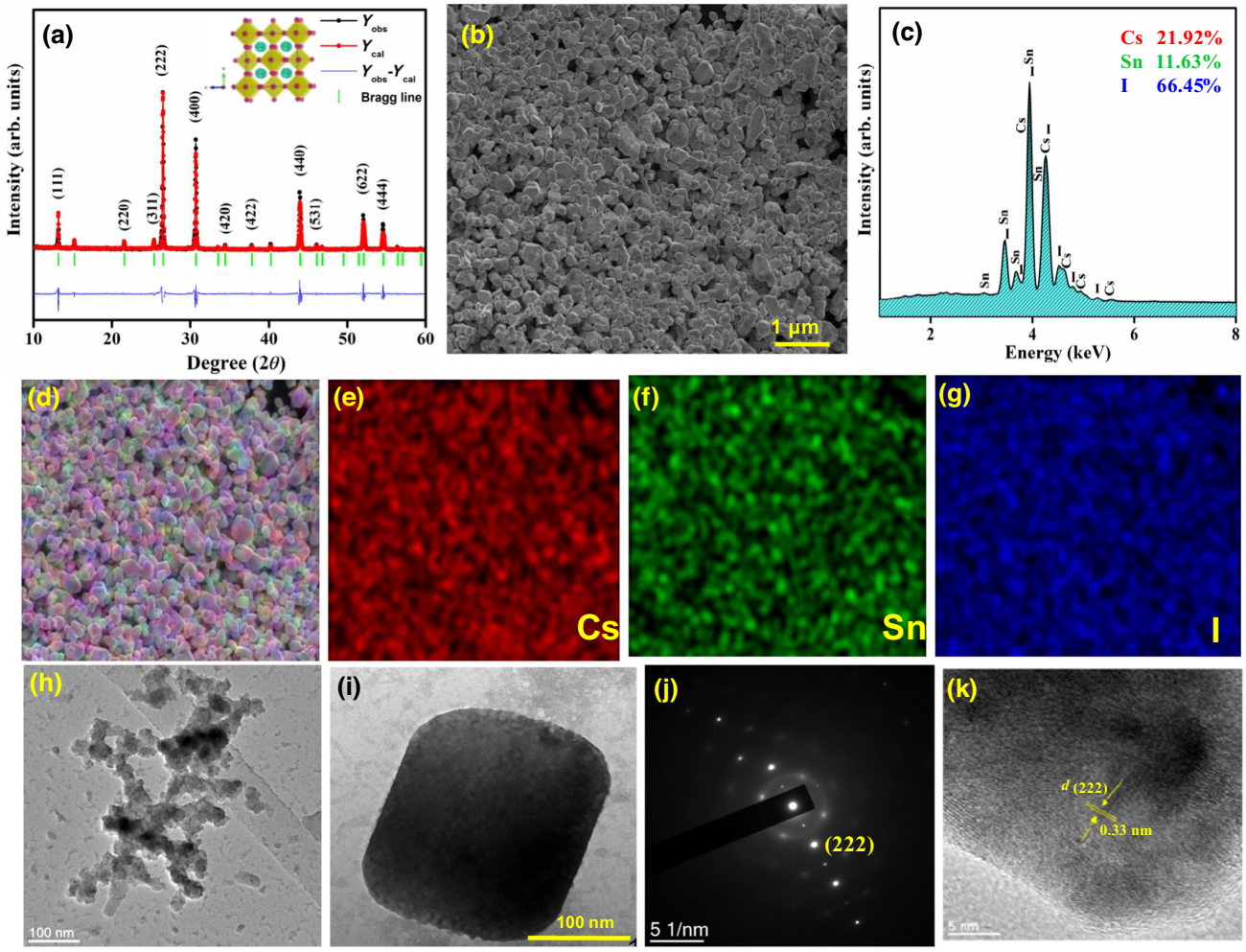

FIG. 1. (a) XRD profile with Rietveld refinement with crystal structure at inset, (b) FESEM image, (c) EDX spectrum, (d)–(g) EDX elemental mapping of Cs_2SnI_6, (h),(i) HRTEM image, (j) SAED pattern of Cs_2SnI_6, and (k) lattice (*d*-spacing) pattern.

demonstrates that the Cs_2SnI_6 perovskite has no impurity phase.

The morphology of Cs_2SnI_6 perovskite as studied by FESEM imaging is displayed in Fig. 1(b). The FESEM image of Cs_2SnI_6 reveals the small particlelike structures with sizes of 50–60 nm over the entire inspected region. The morphological uniformity of the sample is visible in the FESEM image. The elemental composition of the synthesized perovskite was investigated using energy dispersive X-ray (EDX) measurement, and the results are shown in Fig. 1(c). The EDX spectrum of Cs_2SnI_6 shows intense peaks corresponding to Cs, Sn, and I only. No additional peaks related to any impurity were registered in the profile. This result agrees well with the XRD results and substantiates the pure phase formation. The constituent elements show an atomic ratio of approximately 21.92: 11.63: 66.45 (Cs : Sn : I) in the sample, which is in good agreement with the actual stoichiometry. The elemental mapping of these elements over the scanned region [Figs. 1(d)–1(g)] indicates that the elements are distributed uniformly. The TEM images of the Cs_2SnI_6 perovskite are shown in Figs. 1(h) and 1(i), which display small particles with a radius of about 40 nm, indicating that the perovskite is morphologically uniform. The selected area electron diffraction (SAED) pattern of the particle [Fig. 1(j)] with bright circular spots also confirms the single-crystal nature. Furthermore, the HRTEM image [Fig. 1(k)] of the individual particle reveals parallel lattice fringes with an assessed lattice spacing of 0.33 nm, corresponding to the (222) plane of the cubic phase of Cs_2SnI_6, which confirms the single-crystal nature. The diffuse reflectance spectrum of the Cs_2SnI_6 perovskite is shown in Fig. S2 where reflectance (R) is plotted as a function of the photon wavelength λ (nm) within the Supplemental Material [45]. The estimated band-gap value is about 1.50 eV, which is in good agreement with previously published values [52].

X-ray photoelectron spectroscopy (XPS) was employed to investigate the core-level electron binding energies of Cs_2SnI_6 halide perovskite. The peaks of the constituent

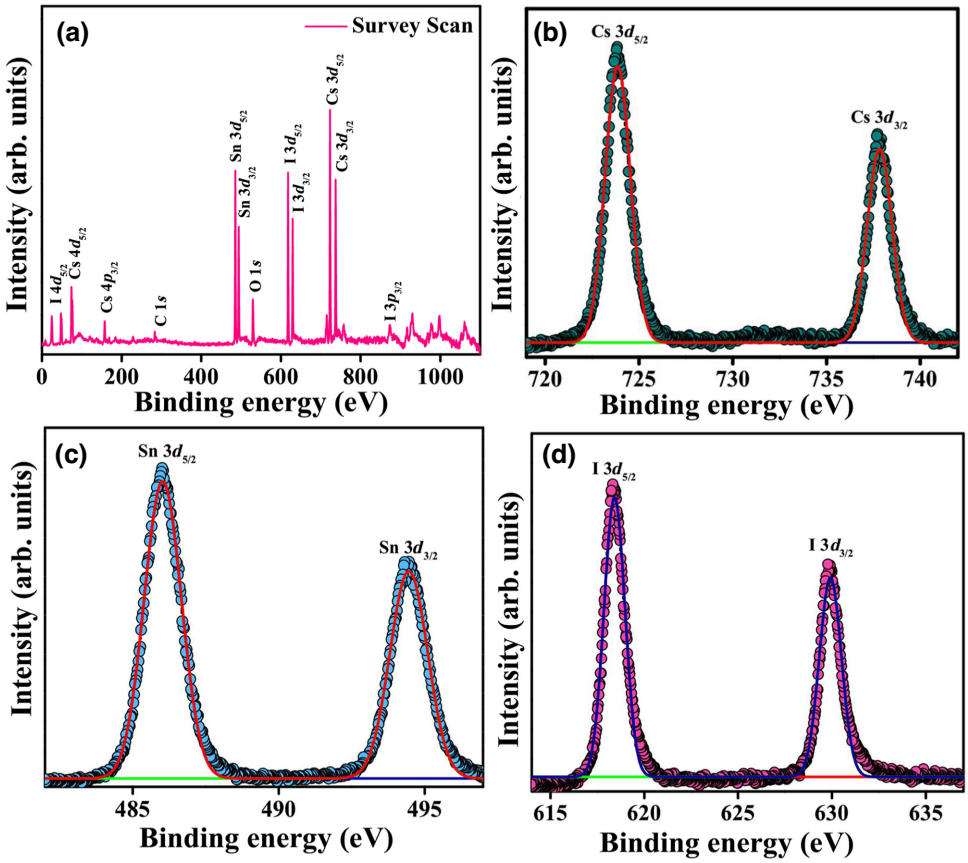

FIG. 2. (a) XPS survey scan and core level XPS spectra of Cs_2SnI_6, (b) Cs, (c) Sn, (d) I.

atoms, namely Cs, Sn, and I originate from the spin-orbit coupling of electronic states. By using the adventitious C 1 s peak at 284.6 eV as a reference point, all binding energies were charge corrected. The survey profile of Cs_2SnI_6 shown in Fig. 2(a) confirms the presence of peaks associated with the constituent elements, i.e., Cs, Sn, and I, corroborating the EDX results. In addition to the sample components, additional C- and O-related peaks resulted from the presence of the ambient carbon and oxygen. The component constituents of Cs_2SnI_6 are represented by core-level spectra in Figs. 2(b)–2(d). In the core-level, Cs 3*d* spectrum shown in Fig. 2(b), the two main peaks that correspond to Cs $3d_{5/2}$ and Cs $3d_{3/2}$, respectively, are located at 723.81 and 737.80 eV. The Sn 4*f* spectrum demonstrated in Fig. 2(c) exhibits doublet characteristics with peaks at 485.97 and 494.37 eV, which are assigned to Sn $3d_{5/2}$ and Sn $3d_{3/2}$, respectively. The peaks associated with I $3d_{3/2}$, and I $3d_{5/2}$ appear at 629.87 and 618.30 eV, respectively [see Fig. 2(d)]. The positioning of the peaks shows that the constituent elements Cs, Sn, and I are in their typical valence states of 1^+, 4^+, and 1^-, respectively. All these results are also in good agreement with the literature [53].

B. Electronic structure of Cs_2SnI_6 using density-functional theory (DFT)

Figures 3(a) and 3(b) show the electronic band structure and DOS. The obtained electronic band gap (E_g) is 0.97 eV, indicating that the gap is direct. However, according to the previous literature, the material is a semiconductor with $E_g \sim 1.2$–1.5 eV. According to a previous report, the band gap for PBE or LDA-based pseudopotentials is underestimated [54]. However, hybrid pseudopotentials provide a more acceptable value, though it may be reduced significantly in the presence of defects or doped elements [54,55]. The electron-density map and electron-localization function (ELF) are provided in Fig. S3 of the Supplemental Material [45]. Considering its symmetry, the phonon band structure is computed along the symmetry path $X \to R \to M \to \Gamma \to R$ and is demonstrated in Fig. 3(c). The density of phonon states as a function of phonon frequency is illustrated in Fig. 3(d). Both results exhibit phonon bands with imaginary phonon energies, especially in the vicinity of the *R* point. Because of the anharmonic rattling of Cs atoms and the dynamical rotation of SnI_6 octahedra [26], this implies the presence of anharmonic phonon soft modes, indicating a dynamic

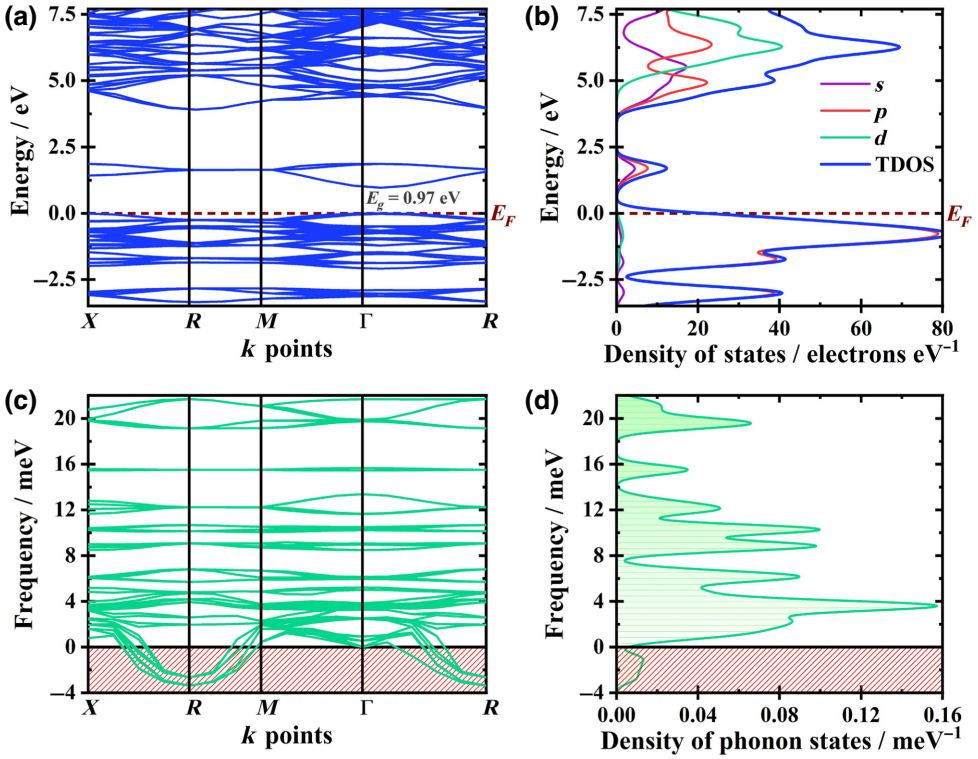

FIG. 3. (a) Electronic band structure, (b) total and projected DOS with orbital contributions, (c) phonon dispersion and (d) density of phonon states for the cubic phase of the Cs_2SnI_6 double perovskite.

instability in the cubic phase of Cs_2SnI_6 double perovskite [56]. The optical dielectric function and relevant thermodynamic parameters were also calculated as a function of temperature and are displayed in Fig. S4 of the Supplemental Material [45].

C. Analysis of complex impedance spectra

Figures 4(a) and 4(b) show the Nyquist plot ($-Z''$ versus Z') of Cs_2SnI_6 perovskite at different temperatures in the temperature ranges 193–323 K and 333–473 K, respectively. Here, the frequency-dependent real and imaginary parts of the complex impedance $Z^*(\omega)$ are represented by $Z'(\omega)$ and $-Z''(\omega)$, respectively, and are defined by $Z^*(\omega) = Z'(\omega) - jZ''(\omega)$. From the Nyquist plots, it is observed that the diameter of the depressed semicircles decreases with increasing temperature. This behavior can be explained by the fact that the dc conductivity of dielectric materials increases with an increase in temperature. The Nyquist plot of Cs_2SnI_6 double perovskite can be characterized by three distinct arcs in the temperature range of 193–323 K arising from the dominance of different factors in different frequency ranges such as rattling-assisted polaron, grain boundaries and grain response at low temperatures. In Cs_2SnI_6, the anharmonic rattling motion of positive Cs^+ and the dynamic motion of negative $[SnI_6]^-$ octahedra create a charge separation in the primitive cell, which form ionic polarization as well as rattling-assisted polarons in this material [26]. The impedance plot in the temperature range of 333–473 K can be described by the two arcs arising from the grain boundaries and grain response, and the electrode polarization effect is observed in the low-frequency region at high temperatures. It should be noticed that the high-frequency arc in the temperature range of 333–473 K is not observed because it is outside the measurement range of our instrument.

The depressed semicircles are fitted using the Maxwell-Wagner equivalent circuit model [57]. Two equivalent circuit models are used to describe the impedance spectra for the two previously mentioned temperature regions; these comprise R-CPE circuits in parallel connection, where R and CPE are resistance and constant phase element, respectively. Z_{CPE} is defined by $Z_{CPE} = 1/A(j\omega)^m$, where ω denotes angular frequency, A is a proportionality constant, and m is an exponent whose value lies between 0 and 1. The value $m = 1$ indicates that the CPE is purely capacitive, and for $m = 0$, the CPE becomes purely resistive.

The three/two parallel R-CPE circuit models were fitted to the Nyquist plots in Figs. 4(a) and 4(b) in various frequency and temperature regions. Resistances and CPEs correspond to grain boundaries, grain and rattling-assisted polaron contributions are denoted by R_1/CPE_1, R_2/CPE_2, and R_3/CPE_3 respectively shown in the inset of these

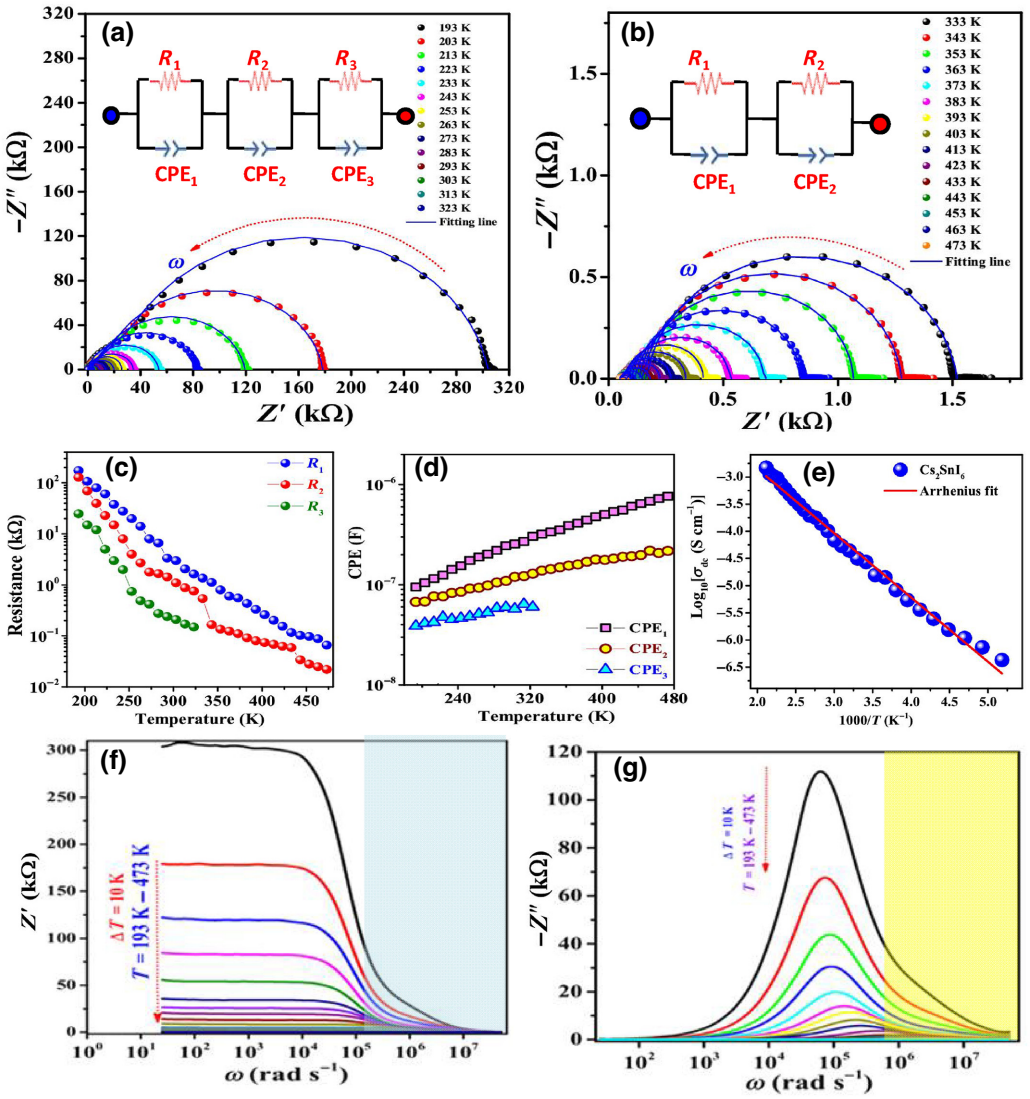

FIG. 4. (a),(b) Complex impedance plots of Cs_2SnI_6 double perovskite at different temperatures. Inset figures show the equivalent circuit model for analyzing the impedance data, (c),(d) temperature dependence of resistance and constant phase element values obtained from equivalent circuit model fitting of experimental data, (e) reciprocal temperature dependence of dc conductivity for Cs_2SnI_6. Frequency dependence of (f) real impedance spectra (Z') and (g) imaginary impedance spectra ($-Z''$).

figures. To study the variation of the resistances (R_1, R_2, and R_3) with temperature, we have plotted those against temperature in Fig. 4(c) from which it can be noted that (i) each of these resistances decreases with increasing temperature, and (ii) the resistance arising from the grain boundary is the highest among the three throughout the entire temperature range. The fall of the resistance values R_1, R_2, and R_3 with increasing temperature is associated with the fact that the conductivity of Cs_2SnI_6 increases owing to the enhanced dynamics of thermally activated behavior. The capacitance values from different contributions, such as grain boundary (CPE_1), grain (CPE_2), and polaron response (CPE_3) obtained from the fits of the Nyquist plots to the equivalent circuit model at different temperatures are shown in Fig. 4(d). For different contributions, the value of the capacitance increases slightly with increasing temperature. The increment of the capacitance values with temperature for grain-boundary contribution indicates that more charge carriers are accumulated near the grain boundaries, performing as a trapper site of more active charge carriers changing the mobility [35]. As the temperature increases, the value of the bulk resistance ($R_b = R_1 + R_2 + R_3$) contributed by grain, grain boundary, polaron contributions decreases for Cs_2SnI_6 perovskite. We have calculated the dc conductivity (σ_{dc}) of the Cs_2SnI_6 perovskite at different temperatures from the impedance plot by using the following relationship: $\sigma_{dc}(T) = t/R_bA$, where t and A are

the thickness and area of the sample pellet, respectively. The Cs_2SnI_6 perovskite shows a dc conductivity value of approximately 3.77×10^{-5} S cm^{-1} at 303 K and the dc conductivity value increases with increasing temperature. Figure 4(e) shows the reciprocal temperature dependence of the dc conductivity, which obeys the Arrhenius relation:

$$\sigma_{dc}(T) = \sigma_0 \exp\left(\frac{-E_\sigma}{k_B T}\right), \quad (1)$$

where σ_0 is the pre-exponential factor, E_σ is the activation energy, and k_B is the Boltzmann constant. The calculated value of the activation energy is approximately 0.153 ($\pm$0.004) eV. The value of the activation energy is much less than the half of the optical band gap reported earlier [54]. This happens due to the presence of polarons arising from the defects present in the materials [54,55].

Figure 4(f) displays the variation of Z' as a function of angular frequency at different temperatures. It is observed in Fig. 4(f) that the magnitude of Z' shrinks with increasing angular frequency and temperature, which is related to the lowering of the barrier height of the space-charge region at the grain boundaries due to the rise in temperature. The appearance of a plateau in the low-frequency region is related to the long-range dynamics of charge carriers, and the decrease of Z' with increasing of temperature reveals the existence of a negative temperature coefficient of resistance in Cs_2SnI_6 perovskite. The negative temperature coefficient of Z' indicates the increase in conductivity with temperature. The Z' displays a gradual decrease as the temperature increases and exhibits a second small plateau region at a high angular frequency region (shaded region) caused by short-range dynamics of the charge carrier and hopping of rattling-assisted polarons. Figure 4(g) depicts the variation of $-Z''$ with angular frequency at different temperatures. It demonstrates existence of the relaxation peaks at different temperatures. Due to charge-carrier dynamics in the low angular frequency region as well as polaron hopping in the high-frequency region, two relaxation peaks appear in the angular frequency dependence of $-Z''$, indicating the presence of thermally activated behavior [58,59].

D. Analysis of ac conductivity spectra

The ac conductivity spectra have been studied to gain a better understanding of the long-range ($\omega \to 0$) and short-range charge-carrier dynamics, and rattling-assisted polaron dynamics for the Cs_2SnI_6 double perovskite. Figure 5(a) represents the ac conductivity spectra in the temperature region of 193–473 K. The ac spectra at low temperatures exhibit two different regions, such as a frequency-independent plateau region and a dispersive region upto 100 kHz. There exists a slope changing dispersive region in the ac conductivity spectra (shaded region) beyond 100 kHz at low temperatures, and this region shifts to the high-frequency side with increasing temperature. This region is not observed at high temperatures due to our instrumental limitations. The plateau region at lower frequencies corresponds to long-range dynamics of charge carriers by hopping process, representing the dc conductivity of the material. The charge-carrier hopping in this region can be treated as charge-carrier motion in an infinite lattice of identical potential wells. The dispersive region up to 100 kHz can be explained with the short-range charge carriers hopping between localized sites, and the hopping mechanism of charge carriers in this region is confined in the double-well potential with infinite potential barriers via forward-backward hopping on either side [60]. The conductivity increases exponentially due to perturbation of the mechanism through the ac electric field [60]. In the higher-frequency dispersive region beyond 100 kHz, the motion of the charge carriers is limited to localized sites and can be caused by the hopping of polarons associated with anharmonic rattling effects in the Cs_2SnI_6 double perovskite. With further increase in frequency, the value of the ac conductivity increases. At higher temperatures, the plateau region of the ac conductivity spectra, i.e., dc conductivity becomes relatively dominant in comparison with lower temperatures, and an electrode polarization effect is slightly observed in the low-frequency region at relatively high temperatures. The transition frequency at which the ac conductivity starts to increase after the dc conductivity region is called the hopping frequency (ω_H). Except the slope-changing dispersive region at high frequencies, the ac conductivity spectra are well fitted to the Jonscher power-law model modified by Almond and West [61,62]. According to this model, the ac conductivity can be expressed as

$$\sigma'(\omega) = \sigma_{dc}\left[1 + \left(\frac{\omega}{\omega_H}\right)^n\right], \quad (2)$$

where σ_{dc} is the dc conductivity, ω_H is the hopping frequency, and n is the power-law exponent. The variation of dc conductivity (σ_{dc}), obtained from the fits, with $1000/T$ shown in Fig. 5(b) follows the Arrhenius relation [Eq. (1)]. Figure 5(b) shows that the values of σ_{dc} derived from the Nyquist plots match well with the σ_{dc} values derived from the ac conductivity spectra. The activation energy (E_σ) for dc conductivity calculated from ac conductivity is approximately 0.149 ($\pm$0.005) eV, which is very close to that of σ_{dc} calculated from the impedance plot. Figure 5(c) illustrates the reciprocal temperature dependence of the hopping frequency obtained from the power-law fits, which also obeys the following Arrhenius relation:

$$\omega_H(T) = \omega_0 \exp\left(\frac{-E_H}{k_B T}\right), \quad (3)$$

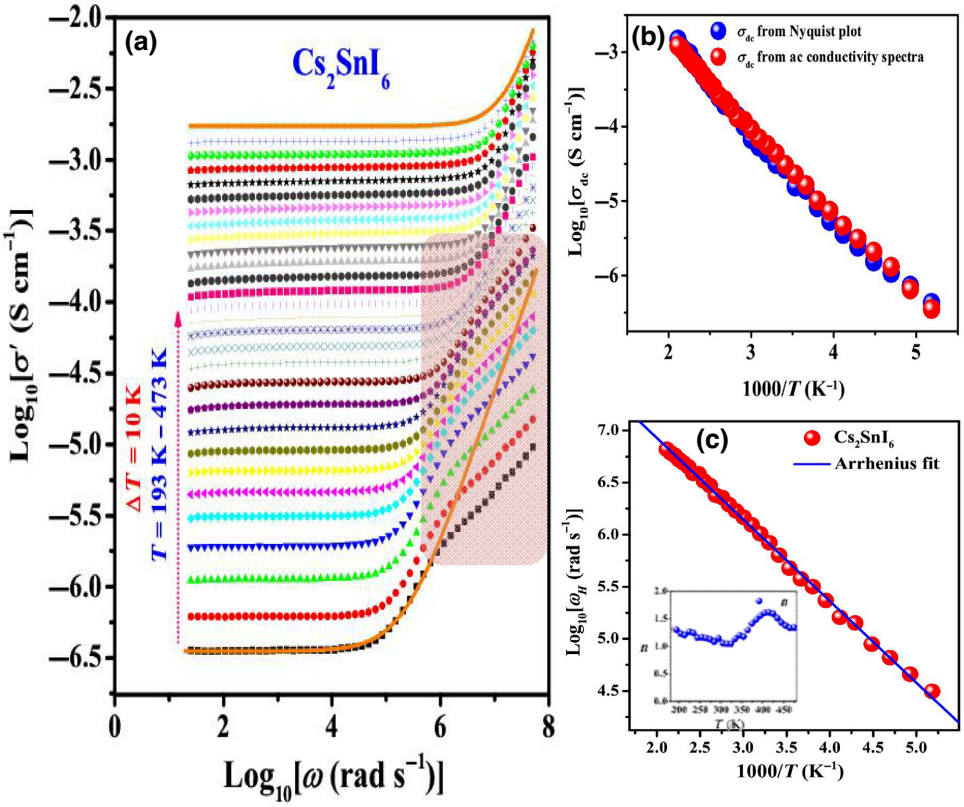

FIG. 5. (a) ac conductivity for Cs_2SnI_6 at different temperatures and solid line is the best fits to Eq. (2). Reciprocal temperature dependence of (b) dc conductivity and (c) hopping frequency for Cs_2SnI_6 perovskite. The inset of (c) represents the temperature variation of the power-law exponent.

where ω_H is the hopping frequency. The solid line in Fig. 5(c) represents the best fit to Eq. (3). The activation energy (E_H) for ω_H is calculated as 0.138 ($\pm$0.006) eV, which is very close to the activation energy obtained for σ_{dc} within experimental errors, indicating a common charge-carrier dynamics and relaxation mechanism in the Cs_2SnI_6 perovskite. The value of the power-law exponent n at different temperatures is shown in the inset of Fig. 5(c). It is observed that the exponent n changes with temperature. Initially, it ($n \sim 1.3$) decreases with temperature, reaching a minimum value ($n \sim 1.05$) at $T = 323$ K and then increasing upto $T = 413$ K where the value of n is approximately 1.6. The value of the exponent decreases further as temperature increases, where the value of $n \sim 1.34$. However, for all temperatures, the value of the power exponent n is greater than unity ($n > 1$), indicating superlinear power-law (SPL) behavior [25]. It is also noted that the slope of the ac conductivity spectra at high frequencies beyond 100 kHz is about 0.52–0.56.

E. Dielectric properties of the Cs_2SnI_6 perovskite

The complex dielectric permittivity $\varepsilon^*(\omega)$ of the Cs_2SnI_6 perovskite is described in terms of real and imaginary parts given by the relation: $\varepsilon^*(\omega) = \varepsilon'(\omega) - j\,\varepsilon''(\omega)$. The real part $\varepsilon'(\omega)$ (known as dielectric constant) represents the stored energy and the imaginary part $\varepsilon''(\omega)$ (known as dielectric loss), is the dissipation of energy or loss factor associated with the polarization process. The frequency dependence of the dielectric constant and dielectric loss can be expressed in terms of impedance by the following relations:

$$\varepsilon'(\omega) = \frac{Z'}{\omega C_0 (Z'^2 + Z''^2)} \text{ and } \varepsilon''(\omega) = \frac{Z''}{\omega C_0 (Z'^2 + Z''^2)}, \tag{4}$$

where $C_0 (\sim (\varepsilon_0 A/t))$ is free-space capacitance, ε_0 is the dielectric permittivity of vacuum, A is the effective electrode area, and t is the thickness of the pellet. Figures 6(a) and 6(b) show the frequency dependence of $\varepsilon'(\omega)$ and $\varepsilon''(\omega)$, respectively, at various temperatures. The figures indicate that at a particular temperature, the values of both $\varepsilon'(\omega)$ and $\varepsilon''(\omega)$ are higher in the lower-frequency region and gradually decrease with increasing frequency. The value of the dielectric constant, i.e., $\varepsilon'(\omega)$ is dominated by orientational and interfacial polarizations in the low-frequency region, while ionic and electronic polarizations govern the dielectric constant in the high-frequency region in consistent with Koop's phenomenological theory [63].

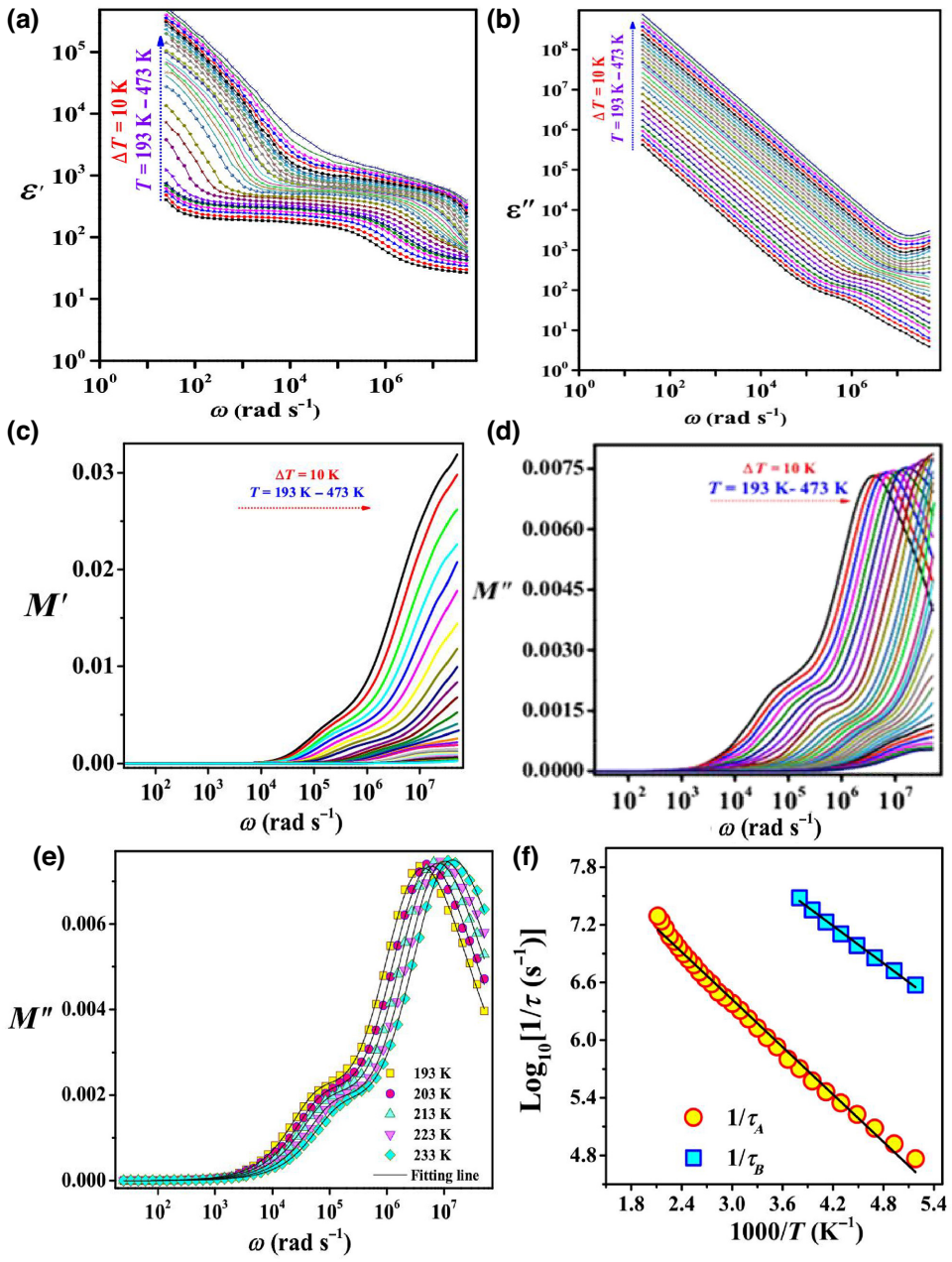

FIG. 6. Frequency dependence of (a) dielectric constant ε' and (b) dielectric loss ε'' at different temperatures, (c) real and (d) imaginary part of complex electric modulus spectra at different temperatures, (e) frequency dependence of imaginary part of complex modulus with fitting of Kohlrausch-Williams-Watts function at $T = 193$ K and (f) reciprocal temperature dependence of inverse relaxation time $(1/\tau)$ and the solid lines are the best fits to Eq. (6).

As the dielectric materials consist of a low-resistive layer of grains that are separated by boundaries of moderately low conductivity, charges accumulate at the grain boundaries, barring charge carriers from moving freely. When an electric field is applied, opposite charges move towards opposite poles, making a large number of dipoles align with the applied electric field. At lower frequencies, these dipoles can easily follow the varying field, resulting in high dielectric permittivity values. With increasing frequency, the dipoles fail to cope with the rapidly changing field, and hence the dielectric constant decreases with increasing frequency. The lower values of the dielectric constant indicate that the dipoles are unable to orient easily as per the applied field at lower temperatures. At higher temperatures, the presence of more thermal energy makes the orientation of the dipoles easy. That is why the values

of the dielectric constant rise as the temperature rises. A shoulderlike feature and a leveling off ε_∞ (the high-frequency limiting value) towards the higher frequencies are observed in the dielectric constant. At a certain value of dielectric constant ε', a single plateaulike feature is observed, denoted as low-frequency static values, εs, which are related to the long-range charge-carrier dynamics, contributing to the dc conductivity. The dielectric relaxation strength $\Delta\varepsilon$ is defined as the difference between the low-frequency static value (ε_s) and the high-frequency limiting value (ε_∞) of the dielectric constant. The dielectric relaxation time (τ) is defined as the reciprocal of the corresponding midfrequency where transitions from static to high-frequency dielectric constant occur. Initially, ε'' decreases monotonically with increasing frequency. It is noted that ε'' tends to follow the relation: $\varepsilon'' \propto f^{-1}$ in the midfrequency region. The dielectric loss ε'' spectra in the very high-frequency region show broad relaxation peaks corresponding to the rattling-assisted polaron response, and the peak positions shift to the high-frequency side with the increase in temperature. At higher temperatures, the peaks were not observed due to our instrumental limitation. The relaxation process associated with charge carriers was not observed in the midfrequency region of ε'' due to the large electrode polarization effect.

The dielectric constant ε' of the material at different temperatures has been fitted using the real part of the Cole-Cole function and a typically fitted curve at $T = 193$ K is shown in Fig. S5(a) within the Supplemental Material [45]. The Cole-Cole function is given by [64]

$$\varepsilon^*(\omega) = \varepsilon_\infty + \frac{\varepsilon_s - \varepsilon_\infty}{1 + (i\omega\tau_{CC})^{1-\alpha}}, \tag{5}$$

where the parameter α is constant for a given material having value $0 \le \alpha \le 1$ and $\alpha = 0$ for Debye relaxation.τ_{CC} is the dielectric relaxation time, ε_s and ε_∞ represents the static and high-frequency dielectric constants, respectively. It may be noted that the relaxation time associated with charge carriers decreases with the increase in temperature, indicting thermally activated dielectric relaxation process. The reciprocal temperature dependence of the inverse dielectric relaxation time ($1/\tau_{CC}$) obtained from the Cole-Cole fits is shown in Fig. S5(b) within the Supplemental Material [45], which follows the Arrhenius relation:

$$\frac{1}{\tau_{CC}(T)} = \frac{1}{\tau_0} \exp\left(\frac{-E_\tau}{k_B T}\right) \tag{6}$$

The activation energy (E_τ) for the relaxation time obtained from the fits is approximation 0.136 ($\pm$0.006), which is comparable with the values of E_σ and E_H. The reciprocal temperature dependence of the static dielectric constant obtained from the fits is shown in the inset of Fig. S5(b) within the Supplemental Material [45], which indicates that its value increases almost linearly with increasing temperature.

The complex electric modulus spectroscopy has been investigated to understand the dielectric relaxation mechanism of the Cs_2SnI_6 perovskite. The complex electric modulus $M^*(\omega)$ is defined as the reciprocal of complex dielectric permittivity:$M^*(\omega) = 1/\varepsilon^*(\omega) = M'(\omega) + jM''(\omega)$, where $M'(\omega)$ and $M''(\omega)$ represent the real and imaginary parts of the complex electric modulus, respectively. The variations of the real part (M') and imaginary part (M'') of the complex modulus data with angular frequency at temperatures ranging from 193 to 473 K are shown in Figs. 6(c) and 6(d), respectively. At all temperatures, $M'(\omega)$ and $M''(\omega)$ saturate to zero in lower angular frequency regions due to suppression of the electrode polarisation, as shown in Figs. 6(c) and 6(d).With increasing angular frequency, the $M'(\omega)$ data increases, showing a shoulder in the midfrequency regions and reaching saturation at high frequencies. On the other hand, the $M''(\omega)$ spectra clearly exhibit two relaxation peaks in the mid- and high-frequency regions at low temperatures. However, at high temperatures the peaks could not be observed in the high-frequency region due to our experimental limitation. The low-intensity relaxation peak of $M''(\omega)$ in the midfrequency region is due to the relaxation process associated with the dynamics of charge carriers, and the high-intensity relaxation peak in the high-frequency region is due to the rattling-assisted polaron relaxation process. It is also noted that as the temperature increases, the relaxation peaks shift to the high-frequency side. The imaginary part $M''(\omega)$ of the complex modulus data has been analyzed by the Kohlrausch-Williams-Watts (KWW) function given by [60,65]

$$M''(\omega) = \frac{(M''_{\max})_A}{(1-\beta_A) + (\beta_A/1+\beta_A)[\beta_A((\omega_{\max})_A/\omega) + (\omega/(\omega_{\max})_A)^{\beta_A}]} + \frac{(M''_{\max})_B}{(1-\beta_B) + (\beta_B/1+\beta_B)[\beta_B((\omega_{\max})_B/\omega) + (\omega/(\omega_{\max})_B)^{\beta_B}]}, \tag{6}$$

where $(M''_{max})_A$ and $(M''_{max})_B$ are the amplitude of the peak of M'' for ionic relaxation (A) and rattling-assisted polaron relaxation (B) and the relaxation frequencies corresponding to two different relaxation processes are denoted as $(\omega_{max})_A$ and $(\omega_{max})_B$. The stretched exponents for the two processes are β_A and β_B ($0 < \beta \leq 1$). For Debye-type relaxation process, the value of the stretched exponent β is unity and decreases with increasing deviation from Debye-type relaxation.

The frequency dependence of the imaginary part of the complex modulus $M''(\omega)$ was fitted to Eq. (6). The best fits at several temperatures are shown in Fig. 6(e). It may be noted that the fits are very good. The relaxation times (τ_A and τ_B) obtained from the best fits are shown in Fig. 6(f) as a function of reciprocal temperature. It is noted that the relaxation times decrease with increasing temperature and the value of the relaxation time (τ_A) for the ionic relaxation process is greater than that for the rattling-assisted polaron-relaxation process. The temperature dependence of relaxation time follows Arrhenius behavior with activation energies $E_A \sim 0.150$ (± 0.040) and $E_B \sim 0.090$ (± 0.040). It is worthy to note that the activation energy (E_A) for ionic relaxation time (τ_A) is very close to that (E_σ) for the dc conductivity, implying that similar ion conduction and relaxation mechanisms exist in these double perovskites. As a result, the complex electric modulus results can be used to investigate the dynamic processes of both ions via hopping and rattling-assisted polarons. Figure S6(a) within the Supplemental Material shows the temperature dependence of the stretched exponent [45]. The value of β_A increases slightly from 0.78 to 0.89 with increasing temperature, indicating a decrease in the number of ions in short-range transport. Because of the decrease in the amount of polarons in the transport process, the values of the stretched exponent β_B increase slightly from 0.51 to 0.58 in the temperature range of 193 to 283 K.

The scaling of the ac conductivity spectra at different temperatures has received great attention to understand the temperature dependence of charge-carrier dynamics in various disordered and crystalline materials [35, 42]. Following the time-temperature superposition (TTS) principle, the scaling of the ac conductivity spectra has been represented by the following relationship: $(\sigma'(\omega, T))/(\sigma_{dc}(T)) = f(\omega/\omega^*)$, where f and ω* represent the scaling function and scaling parameter, respectively, as proposed by Ghosh and Pan [66]. Here, following this relation we have scaled the conductivity axis $\sigma'(\omega)$ by σ_{dc} and the frequency axis by the hopping frequency (ω_H) at different temperatures. The result is illustrated in Fig. S6(b) within the Supplemental Material for Cs_2SnI_6 perovskite [45].The superposition of all ac conductivity spectra at various temperatures on a single master curve up to 100 kHz reveals that the charge-carrier dynamics involved in this double perovskite follows the TTS principle in this frequency range. It should be noted that the contribution of rattling-assisted polaron dynamics explains why the ac conductivity spectra in the high-frequency range do not lie on a single master curve.

F. Electrochemical performance of the Cs_2SnI_6 perovskite in a supercapacitor

The electrochemical behavior of the synthesized Cs_2SnI_6 perovskite is examined in the three-electrode configuration due to its high ionic conductivity at room temperature. Figure 7(a) represents the schematic model for energy storage using the C_2SnI_6 perovskite as the working electrode. The CV curves at different scan rates for the Cs_2SnI_6 electrode are shown in Fig. 7(b). The Cs_2SnI_6 perovskite exhibits a reversible redox mechanism at the electrode and electrolyte interface and no significant changes in the shape of CV curves are observed even at higher scan rates due to intercalation and deintercalation of ions to the active sites of the working Cs_2SnI_6 electrode [67,68]. The specific capacitance value (C_s^{CV}) of the perovskite electrode was calculated from the CV curve using the following equation:

$$C_s^{CV}(Fg^{-1}) = \frac{\int idV}{\Delta V \times s \times m}, \tag{7}$$

where $\int idV$, ΔV, s, and m represent the area under the CV curve, the potential window (V), the scan rate (mV s^{-1}) and active mass of the working electrode (g), respectively. The variation of the specific capacitance (C_s^{CV}) with the scan rate is shown in Fig. 7(c). The specific capacitances of the perovskite-based supercapacitors are 2375, 1365, 823, 463, 204, 140, and 106 F g^{-1} at the scan rates of 2, 5, 10, 20, 50, 75, and 100 mV s^{-1}, respectively at room temperature. The very high specific capacitance (approximately 2375 F g^{-1} at 2 mV s^{-1}) of perovskite-based supercapacitor decreases gradually with increasing scan rates due to the faster ion movement at higher scan rates. The galvanometric charge-discharge (GCD) profiles for Cs_2SnI_6 at different current densities of 2, 4, 6, 8, 10, and 15 A g^{-1} are displayed in Fig. 7(d), which shows a very prominent nonlinearity in the shapes of the discharge profiles of the Cs_2SnI_6 perovskite electrode. The value of the specific capacitance C_s^{GCD} was further determined from the galvanometric charge-discharge (GCD) profiles using the following relation:

$$C_s^{GCD}(Fg^{-1}) = \frac{i\Delta t}{m \times \Delta V}, \tag{8}$$

where i (A) denote the discharging current, and Δt (s) denotes the discharge time. ΔV (V) is the voltage window, and m (g) is the active mass of the electrode. The variation of the C_s^{GCD} values at different current densities for the fabricated electrode is shown in Fig. 7(e). The calculated values of C_s^{GCD} from each GCD profile are 3830, 2187,

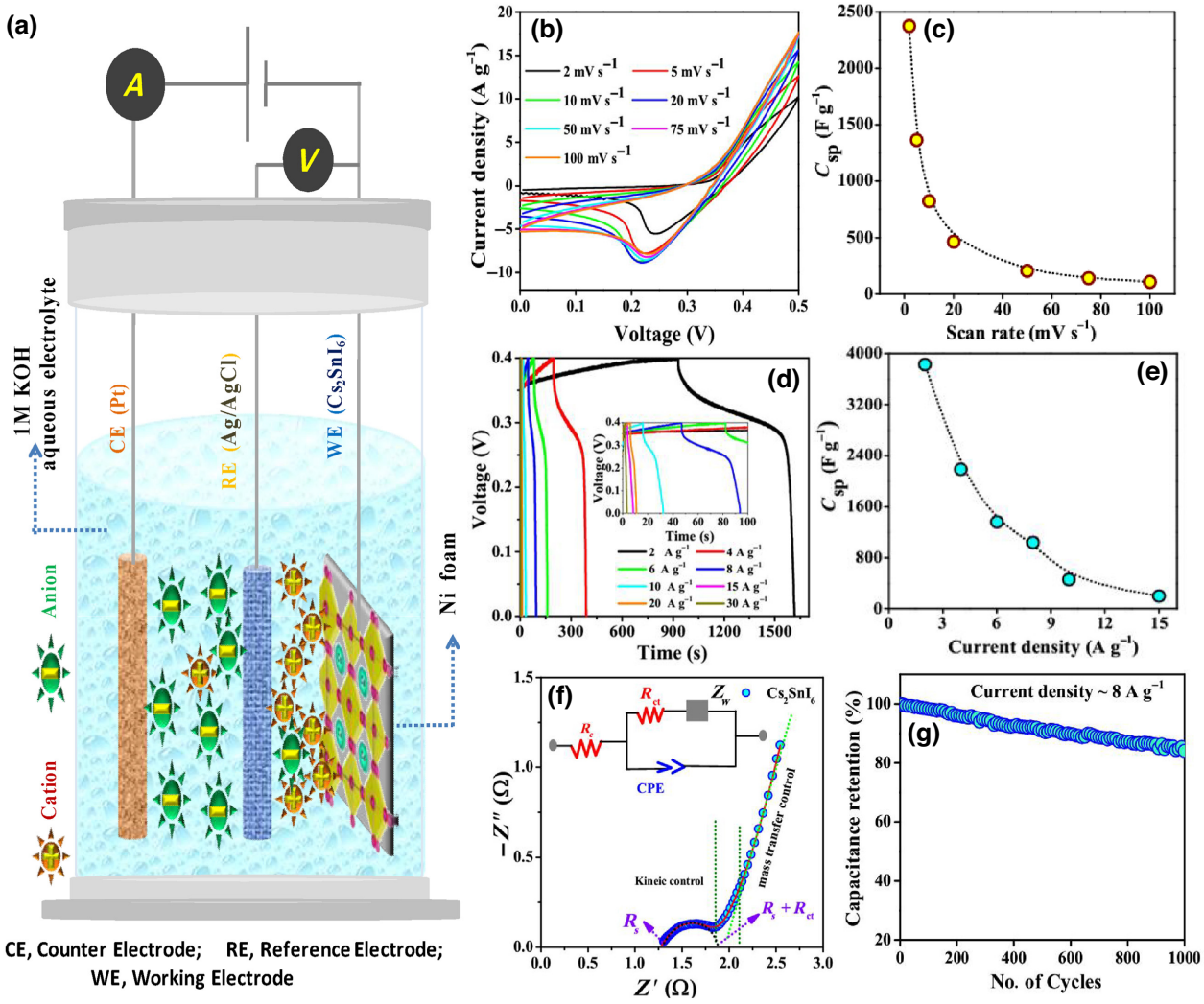

FIG. 7. (a) Schematic model representing energy storage in Cs_2SnI_6 electrode, (b) CV curves at different scan rates, (c) plot of specific capacitance values derived from CV as a function of scan rate, (d) GCD curves for Cs_2SnI_6 as a function of current density, (e) specific capacitance values derived from GCD at different current densities, (f) Nyquist plot with equivalent circuit for Cs_2SnI_6 perovskite electrode and (g) capacitance retention (%) at current density 8 A g^{-1}.

1363, 1041, 462, and 199 F g^{-1} at current densities of 2, 4, 6, 8, 10, and 15 A g^{-1}, respectively, at room temperature. A gradual decrease of specific capacitance with increasing current densities is observed, confirming a good agreement between the GCD and CV results.

The electrolyte resistance, charge-transfer resistance, and ion diffusion process of the Cs_2SnI_6 electrode have also been investigated using the electrochemical impedance spectroscopic measurement. The initial Nyquist plot in the frequency range of 10 mHz to 100 kHz at room temperature, shown in Fig. 7(f), is composed of a semicircular curve at high frequencies that corresponds to the Faradic interfacial charge-transfer resistance (R_{CT}) and an inclined line at low frequencies, which is related to the Warburg resistance (Z_W) [69]. We have used the equivalent circuit model shown in the inset of Fig. 7(f) to fit the impedance data, and the total impedance (Z_T) can be expressed as

$$Z_T = Z_{R_e} + \frac{1}{Z_{\mathrm{CPE}} + [1/(Z_{R_{\mathrm{ct}}} + Z_w)]}. \tag{9}$$

The lower value of charge-transfer resistance (R_{ct} ~ 0.53 Ω) obtained from the above fitting indicates efficient charge transfer at the electrode-electrolyte interface. We have recorded the impedance data after 1000 cycles shown in Fig. S7(a) within the Supplemental Material [45]. It is observed that the charge-transfer resistance (R_{ct}) slightly increases to 0.85 Ω. Actually, the Nyquist plot just has a Warburg element consisting of a inclined line with a 45° slope in low frequencies when the mass-transfer process is much slower than the charge-transfer process

corresponding to low R_{ct} value, whereas the semicircular region at high frequencies will dominate the Nyquist plot when the Faradaic reactions are kinetically slow corresponding to high R_{CT} value as well as the Warburg inclined line will not be visible [70]. Thus, the impedance curve of this electrode reveals its hybrid combination of the redox reaction kinetics and the ion-diffusion process. However, the inclined line in the low frequencies of the impedance plot is endorsed to the ionic diffusion into the Cs_2SnI_6 electrode and the Warburg coefficient (σ_w) can be expressed as

$$Z' = R_e + R_{ct} + \sigma_w \omega^{-0.5}, \tag{10}$$

where R_e and R_{ct} denote the electrolyte and charge-transfer resistances, respectively. Figure S7(b) within the Supplemental Material shows the linear plot of Z' versus the reciprocal square root of the angular frequencies ($\omega^{-0.5}$) for the Cs_2SnI_6 perovskite, which was fitted to Eq. (10) in Fig. S7(b) within the Supplemental Material using linear least-squares fits [45]. We have calculated the value of the ionic diffusion coefficient (oxidant and reductant species) of the Cs_2SnI_6 material using the value of the Warburg coefficient ($\sigma_w = 0.089$ cm^2 s$^{0.5}$) obtained from the above fit. The ionic diffusion coefficient can be determined using the following relation [69,71]:

$$D_{ion} = 0.5\left(\frac{RT}{AF^2\sigma_w C}\right)^2, \tag{11}$$

where R is the universal gas constant, T is absolute temperature (303 K), A is the effective surface area of the electrode (0.5 cm^2), F is Faraday's constant (96 500 C mol^{-1}), and C is the molar concentration of ions. We have found a very high value of the ionic diffusion coefficient ($D_{ion} \sim 1.84 \times 10^{-5}$ cm^2 s^{-1}) for Cs_2SnI_6 perovskite at room temperature. Actually, the ion transport from electrolyte to the electrode is a key factor to improve the performance of the supercapacitors [72]. For practical purposes, cyclic stability is a vital parameter to sustain and Fig. 7(g) displays the capacitive retention plot of the device over 1000 charging-discharging cycles at 8 A g^{-1}. The device retained approximately 85% of its initial capacitance value even after 1000 long cycles of operation. The stable high-crystalline quality, strong ionic conductivity, high ion diffusion behavior exhibited by the present Cs_2SnI_6 perovskite electrode is favorable for the superior electrochemical energy-storage performance as well as the notable specific capacity retention of the supercapacitors.

A quasi-solid-state asymmetric supercapacitor has been fabricated using a Cs_2SnI_6 perovskite electrode, activated carbon (AC) electrode, and PVA-KOH-DI water gel polymer electrolyte. Figure 8(a) represents a digital photograph of the fabricated device, including a schematic diagram of the device. The two electrodes (Cs_2SnI_6 and AC) are pasted together with the help of gel polymer electrolyte, keeping cellulose filter paper between them as a separator. Electrochemical measurements such as CV, GCD, and electrochemical impedance of the device are carried out to investigate its electrochemical performance. Figure 8(b) shows the CV curves of the AC electrode and Cs_2SnI_6 electrode at a scan rate of 2 mV s^{-1} in the potential range of -1 to 0 V and -0 to 0.5 V, respectively. The CV curves of the perovskite based asymmetric supercapacitor device at different voltage windows at a scan rate of 30 mV s^{-1} are shown in Fig. 8(c), and the quasirectangular shape of the CV curves remains unchanged at higher voltage windows. Figure 8(d) shows the CV performance of the asymmetric device for different scan rates. It is observed that the shapes of the CV curves remain the same with scan rates, indicating good reversibility as well as a good capacitive nature. The current density increases gradually with the increase in scan rates. The values of the specific capacitances (C_{sp}^{CV}) calculated from CV curves are 262, 168, 113, 80, 62, and 60 F g^{-1} at scan rates of 5, 15, 30, 50, 75, and 100 mV s^{-1}, respectively. It is found that the specific capacitance values decrease with an increase in scan rates for the device. Figure 8(e) shows the galvanostatic charge-discharge (GCD) curves of the device at several current densities in the voltage range of 0–1.5 V. The variation of specific capacitance (C_{sp}^{dis}) value calculated from the GCD curve is shown in Fig. 8(f). It may be noted that the asymmetric device delivered specific capacitance of 163 F g^{-1} at a current density of 1 A g^{-1}. The decrease of capacitance values with current densities is linked to a diffusion-limited charge-transfer process. The superior electrochemical performance of the asymmetric supercapacitor, marked in the Ragone plot, corresponds to a relationship between specific energy density and specific power density. The values of the specific energy density (E) and specific power density (P) of the device have been calculated from GCD curves at different current rates by using the following relations:

$$E(\text{Wh kg}^{-1}) = \frac{C_{sp}^{dis} \times (\Delta V)^2}{2 \times 3.6} \text{ and } P(\text{W kg}^{-1}) = \frac{E \times 3600}{\Delta t}, \tag{12}$$

where ΔV is the working voltage window of the device in the discharge process and Δt symbolizes discharging time. The calculation of energy density and power density has been listed in Table SI in detail within the Supplemental Material [45]. Figure 8(g) displays the Ragone plot of the device, which delivered an energy density of 51 Wh kg^{-1} and a power density as high as 852 W kg^{-1} at a current density of 1 A g^{-1}. Figure 8(h) shows the capacity retention of the fabricated device at a current density of 5 A g^{-1}. It is observed that the capacity retention decreases gradually with increasing cycle numbers and reaches 72%

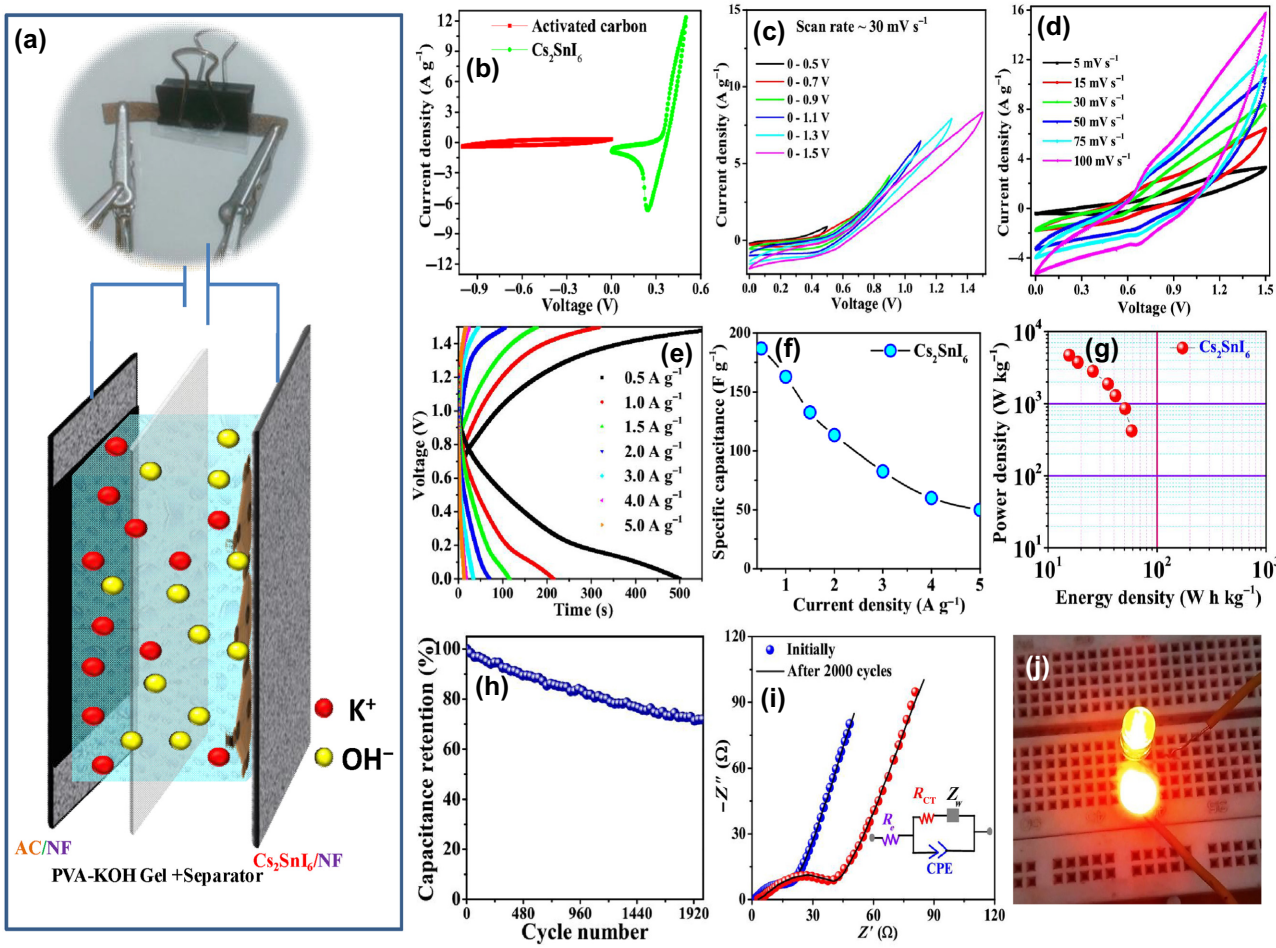

FIG. 8. (a) Digital image and schematic diagram of a single asymmetry supercapacitor device, CV curves of (b) activated carbon and Cs_2SnI_6 perovskite at 2 mV s^{-1} in three-electrode configuration, (c) asymmetric supercapacitor device at different voltage ranges, (d) asymmetric supercapacitor at different scan rates, (e) galvanostatic charge-discharge profiles of the asymmetric supercapacitor at different current densities, (f) specific capacitances of the asymmetric supercapacitor at different current densities, (g) Ragone plot of asymmetric supercapacitor device, (h) capacity retention at current density 5 A g^{-1}, (i) Nyquist plots with equivalent circuit model fits of the device for initially and after 2000 cycles, and (j) snapshots of the glowing LEDs by the fabricated device.

capacity retention at the 2000th cycle. The electrochemical impedance plot (Nyquist plot) of the device before and after 2000 cycles is shown in Fig. 8(i). It is noted that the device displays nearly similar behavior in both cases. The impedance data is fitted with an equivalent circuit model shown in the inset of Fig. 8(i). The electrolyte resistance (R_e) corresponding to the high-frequency region of the device changed from 2 to 3.6 Ω after 2000 galvanostatic charge-discharge cycles. Simultaneously, the charge-transfer resistance (R_{CT}) value also increases initially from 19.7 to 41 Ω after the 2000 galvanostatic charge-discharge cycles' operation due to the loss of binding strength of the PVA polymer. For the commercial utility test, the series combination of two fabricated asymmetric devices charged up to 3.0 V with 20-mA current is capable of powering commercial red LEDs, and a digital image is shown in Fig. 8(j).

The specific capacitance of the Cs_2SnI_6 double-perovskite electrode-based supercapacitor is compared with the recently reported halide perovskites in Table I [73–88]. It is worth mentioning that the reported supercapacitors based on perovskite electrodes have not been studied under the same conditions in terms of size, morphology of the perovskites, electrolytes, etc. However, this investigation provides direct evidence that the Cs_2SnI_6 perovskite electrode for supercapacitors reported in the present study shows superior performance in terms of specific capacitance and energy density. It is worth noting that the metal halide perovskites have received great attention as promising solar-cell materials [89,90]. However, scientists worldwide have recently focused on exploring the electrochemical energy-storage behavior of these halide perovskites in energy-storage devices, such as supercapacitors, Li-ion batteries (LIBs), dual-ion batteries (DIBs), etc.

TABLE I. Comparison of capacitance of the recently reported halide perovskites that are used in the supercapacitor as the electrode.

Sl. No.	Perovskites	Area/specific capacitance	Scan rate/charge-discharge current	Stability (cycle)	Ref.
1	$CH_3NH_3PbI_3$	432 mF cm^{-2}	5 mA cm^{-2}	7	[73]
2	$CsPbI_3$	7.23 mF cm^{-2}	2 mV s^{-1}	1000	[74]
3	$CsPbBr_{2.9}I_{0.1}$	150 mF cm^{-2}	0.1 mA cm^{-2}	2000	[75]
4	$CsPbBr_3$	121 F g^{-1}	5 mV s^{-1}	5000	[76]
5	$CH_3NH_3PbBr_3$	81.5 mFm^{-2}	5 mV s^{-1}	1000	[77]
6	$CH_3NH_3PbI_3$	21.50 μFcm^{-2}	50 mV s^{-1}	1000	[78]
7	$CH_3NH_3PbBr_3$	36.82 F g^{-1}	0.6 mA cm^{-2}	1000	[79]
8	$(CH_3NH_3)_3Bi_2I_9$	5.5 mF cm^{-2}	2 mA cm^{-2}	10 000	[80]
9	$(CN_2SH_5)_3BiI_6$	1030 F g^{-1}	0.44 A g^{-1}	5000	[81]
10	$CH_3NH_3PbI_3$	3.68 μFcm^{-2}	20 mV s^{-1}	10 000	[82]
11	Methylammonium bismuth Triiodide	0.28 mF cm^{-2}	10 mV s^{-1}	5000	[83]
12	$Cs_3Bi_2I_9$	280 F g^{-1}	0.05 A g^{-1}	5000	[84]
13	$Cs_2AgBiBr_6$	55 F g^{-1}	0.2 A g^{-1}	1500	[85]
14	$SrCo_{0.9}$ $Mo_{0.1}O_3$	1223.34 F g^{-1}	1 A g^{-1}	5000	[86]
15	$PrBaMn_2O_{6-\delta}$	1034.8 F g^{-1}	1 A g^{-1}	5000	[87]
16	Cu-Ni-Co based trimetallic oxide	2535 F g^{-1}	1 A g^{-1}	5000	[88]
17	**Cs_2SnI_6**	**3830 F g^{-1}**	**2 A g^{-1}**	**1000 cycles**	**This work**
		2375 F g^{-1}	2 mV s^{-1}		

[37,41,91]. Recently, Li-ion capacitors (LICs), which combine battery and electrochemical capacitors to achieve high energy density, have also received much attention [92]. Due to environmental impact and carbon emissions, world scientists are currently designing alternative energy storage units, termed photobatteries and photosupercapacitors, bridging between dual properties such as energy harvesting and storing energy in devices [39,93]. Our findings show that the as-synthesized Cs_2SnI_6 perovskite has good optical features and has a high energy-storage capability. By employing this perovskite as an electrode material, it may be feasible to fabricate photosupercapacitors and photobatteries to replace conventional LIBs, DIBs, LICs, etc., in the future.

IV. CONCLUSIONS

In summary, we have reported the synthesis, characterization, optical, temperature-dependent dielectric properties, electronic structure, and electrochemical measurements of the cubic phase Cs_2SnI_6 perovskite of the $Fm\bar{3}m$ space group with a lattice constant of 11.644 Å and investigated the physics behind its charge-carrier dynamics and superior energy-storage behavior. The density of phonon states as a function of phonon frequency has also been computed and implies the existence of anharmonic phonon soft modes due to the anharmonic rattling of Cs atoms and the dynamical rotation of SnI_6 octahedra. A quantitative analysis of complex impedance spectra was performed to account for the contribution of grain boundaries, grains, and rattling-assisted polaron response to charge-carrier dynamics. The value of power-law exponent n for all temperatures suggests superlinear power-law (SPL) behavior of ac conductivity in Cs_2SnI_6 perovskite. The dc conductivity derived from impedance spectra, the hopping frequency obtained from ac conductivity, and the dielectric relaxation time derived from dielectric response correspond to charge-carrier dynamics as well as the hopping of anharmonic rattling-assisted polaron responses, which follow the Arrhenius relation. The Cs_2SnI_6 double perovskite exhibits good dc conductivity at 303 K. The relaxation peak of $M''(\omega)$ in the midfrequency region is due to the relaxation process associated with charge-carrier dynamics, and the relaxation peak in the high-frequency region is associated with the rattling-assisted polaron relaxation process. The fabricated supercapacitor using Cs_2SnI_6 perovskite as the working electrode achieves specific discharge capacitances of 3830, 2187, 1363, 1041, 462, and 199 F g^{-1} at the different current densities of 2, 4, 6, 8, 10, and 15 A g^{-1}, respectively, due to its high ionic conductivity (3.77×10^{-5} S cm^{-1} at 303 K) as well as high ionic diffusion coefficient value ($D_{ion} \sim 1.84 \times 10^{-5}$ cm^2 s^{-1}). An asymmetric supercapacitor with a configuration of AC/PVA-KOH gel plus separator/Cs_2SnI_6 perovskite delivers an energy density of 51 W h kg^{-1} at a power density of 852 W kg^{-1} at a current density of 1 A g^{-1}. Commercial red LEDs could be powered by connecting two fabricated asymmetric supercapacitor devices in series. Such a perovskite-based supercapacitor with admirable electrochemical performance suggests its prospects as a building unit for long-term energy-storage devices.

ACKNOWLEDGMENTS

M. Ghosh (File No.: 09/096(1025)/2020-EMR-I) and S. Bhattacharjee (File No.: 09/096(0946)/2018-EMR-I) would like to acknowledge the Council of Scientific and Industrial Research, Govt. of India for the fellowship. The authors also wish to thank the University Grant Commission, Government of India, for the "University with potential for excellence" scheme. P. Pal is grateful to NPDF scheme of Science and Engineering Research Board, Govt. of India, for postdoctoral research fellowship (File No.: PDF/2021/001095). A. Ghosh acknowledges DAE, Govt. of India for Raja Ramanna Fellowship grant.

[1] A. Kojima, K. Teshima, Y. Shirai, and T. Miyasaka, Organometal halide perovskites as visible-light sensitizers for photovoltaic cells, J. Am. Chem. Soc. **131**, 6050 (2009).

[2] R. Wang, T. Huang, J. Xue, J. Tong, K. Zhu, and Y. Yang, Prospects for metal halide perovskite-based tandem solar cells, Nat. Photonics **15**, 411 (2021).

[3] Q. Wang, N. Phung, D. Di Girolamo, P. Vivo, and A. Abate, Enhancement in lifespan of halide perovskite solar cells, Energy Environ. Sci. **12**, 865 (2019).

[4] M. Ahmadi, T. Wu, and B. Hu, A review on organic-inorganic halide perovskite photodetectors: device engineering and fundamental physics, Adv. Mater. **29**, 1605242 (2017).

[5] N. Besra, K. Sardar, S. Maiti, P. K. Sarkar, T. Paul, S. Thakur, G. Majumdar, and K. K. Chattopadhyay, Incorporation of V_2O_5 nanorods into perovskite photodetectors as an alternative approach to enhance device performance: A step towards stability against ambient water species, Dalton Trans. **49**, 15788 (2020).

[6] X.-K. Liu, W. Xu, S. Bai, Y. Jin, J. Wang, R. H. Friend, and F. Gao, Metal halide perovskites for light-emitting diodes, Nat. Mater. **20**, 10 (2021).

[7] T. Paul, P. K. Sarkar, S. Maiti, and K. K. Chattopadhyay, Multilevel programming and light-assisted resistive switching in a halide-tunable all-inorganic perovskite cube for flexible memory devices, ACS Appl. Electron. Mater. **2**, 3667 (2020).

[8] A. Siddik, P. K. Haldar, T. Paul, U. Das, A. Barman, A. Roy, and P. K. Sarkar, Nonvolatile resistive switching and synaptic characteristics of lead-free all-inorganic perovskite-based flexible memristive devices for neuromorphic systems, Nanoscale **13**, 8864 (2021).

[9] T. Paul, P. K. Sarkar, S. Maiti, A. Sahoo, and K. K. Chattopadhyay, Solution-processed light-induced multilevel non-volatile wearable memory device based on $CsPb_2Br_5$ perovskite, Dalton Trans. **51**, 3864 (2022).

[10] A. Sahoo, T. Paul, N. H. Makani, S. Maiti, and R. Banerjee, High piezoresponse in low-dimensional inorganic halide perovskite for mechanical energy harvesting, Sustainable Energy Fuels **6**, 4484 (2022).

[11] T. Paul, S. Maiti, U. Mukherjee, S. Mondal, A. Sahoo, and K. K. Chattopadhyay, Cube shaped $FAPbBr_3$ for piezoelectric energy harvesting devices, Mater. Lett. **301**, 130264 (2021).

[12] S. Mondal, S. Maiti, T. Paul, A. Sahoo, S. Bhattacharjee, N. S. Das, and K. K. Chattopadhyay, All-inorganic halide perovskite tuned robust mechanical-energy harvester: Self driven posture monitor and power source for portable electronics, Appl. Mater. Today **26**, 101385 (2022).

[13] J. You, L. Meng, T.-B. Song, T.-F. Guo, Y. Yang, W.-H. Chang, Z. Hong, H. Chen, H. Zhou, Q. Chen, Y. Liu, and N. De Marco, Improved air stability of perovskite solar cells via solution-processed metal oxide transport layers, Nat. Nanotechnol. **11**, 75 (2016).

[14] W. Li, W. Zhang, S. Van Reenen, R. J. Sutton, J. Fan, A. A. Haghighirad, M. B. Johnston, L. Wang, and H. J. Snaith, Enhanced UV-light stability of planar heterojunction perovskite solar cells with caesium bromide interface modification, Energy Environ. Sci. **9**, 490 (2016).

[15] V. Pecunia, L. G. Occhipinti, A. Chakraborty, Y. Pan, and Y. Peng, Lead-free halide perovskite photovoltaics: Challenges, open questions, and opportunities, APL Mater. **8**, 100901 (2020).

[16] N. K. Noel, S. D. Stranks, A. Abate, C. Wehrenfennig, S. Guarnera, A.-A. Haghighirad, A. Sadhanala, G. E. Eperon, S. K. Pathak, M. B. Johnston, A. Petrozza, L. M. Herz, and H. J. Snaith, Lead-free organic–inorganic tin halide perovskites for photovoltaic applications, Energy Environ. Sci. **7**, 3061 (2014).

[17] P.-P. Sun, Q.-S. Li, L.-N. Yang, and Z.-S. Li, Theoretical insights into a potential lead-free hybrid perovskite: substituting Pb^{2+} with Ge^{2+}, Nanoscale **8**, 1503 (2016).

[18] F. Hao, C. C. Stoumpos, D. H. Cao, R. P. H. Chang, and M. G. Kanatzidis, Lead-free solid-state organic–inorganic halide perovskite solar cells, Nat. Photonics **8**, 489 (2014).

[19] Y. El Ajjouri, V. S. Chirvony, N. Vassilyeva, M. Sessolo, F. Palazon, and H. J. Bolink, Low-dimensional non-toxic $A_3Bi_2X_9$ compounds synthesized by a dry mechanochemical route with tunable visible photoluminescence at room temperature, J. Mater. Chem. C **7**, 6236 (2019).

[20] Y. Chu, Y. Hu, and Z. Xiao, First-principles insights into the stability difference between ABX_3 halide perovskites and their A_2BX_6 variants, J. Phys. Chem. C **125**, 9688 (2021).

[21] J. C.-R. Ke, D. J. Lewis, A. S. Walton, B. F. Spencer, P. O'Brien, A. G. Thomas, and W. R. Flavell, Ambient-air-stable inorganic Cs_2SnI_6 double perovskite thin films via aerosol-assisted chemical vapour deposition, J. Mater. Chem. A **6**, 11205 (2018).

[22] B. Lee, A. Krenselewski, S. I. Baik, D. N. Seidman, and R. P. H. Chang, Solution processing of air-stable molecular semiconducting iodosalts, $Cs_2SnI_{6-x}Br_x$, for potential solar cell applications, Sustainable Energy Fuels **1**, 710 (2017).

[23] Z. Mallick, D. Saini, R. Sarkar, T. K. Kundu, and D. Mandal, Piezo-phototronic effect in highly stable lead-free double perovskite Cs_2SnI_6-PVDF nanocomposite: Possibility for strain modulated optical sensor, Nano Energy **100**, 107451 (2022).

[24] N. K. Tailor, N. Parikh, P. Yadav, and S. Satapathi, Dielectric relaxation and polaron hopping in $Cs_2AgBiBr_6$ halide double perovskites, J. Phys. Chem. C **126**, 10199 (2022).

[25] R. Kumar, P. Srivastava, T. Kumar, and M. Bag, Electronic-ionic transport in $MAPbBr_3$ single crystal: The evidence of super-linear power law in AC conductivity, J. Phys. Chem. C **126**, 14305 (2022).

[26] A. Bhui, T. Ghosh, K. Pal, K. Singh Rana, K. Kundu, A. Soni, and K. Biswas, Intrinsically low thermal conductivity in the n-type vacancy-ordered double perovskite Cs_2SnI_6: Octahedral rotation and anharmonic rattling, Chem. Mater. **34**, 3301 (2022).

[27] K. Miyata, T. L. Atallah, and X.-Y. Zhu, Lead halide perovskites: Crystal-liquid duality, phonon glass electron crystals, and large polaron formation, Sci. Adv. **3**, e1701469 (2017).

[28] D. Ghosh, E. Welch, A. J. Neukirch, A. Zakhidov, and S. Tretiak, Polarons in halide perovskites: A perspective, J. Phys. Chem. Lett. **11**, 3271 (2020).

[29] A. E. Maughan, A. M. Ganose, A. M. Candia, J. T. Granger, D. O. Scanlon, and J. R. Neilson, Anharmonicity and octahedral tilting in hybrid vacancy-ordered double perovskites, Chem. Mater. **30**, 472 (2018).

[30] Z. Xiao, Y. Yuan, Y. Shao, Q. Wang, Q. Dong, C. Bi, P. Sharma, A. Gruverman, and J. Huang, Giant switchable photovoltaic effect in organometal trihalide perovskite devices, Nat. Mater. **14**, 193 (2014).

[31] D. Li, H. Wu, H.-C. Cheng, G. Wang, Y. Huang, and X. Duan, Electronic and ionic transport dynamics in organolead halide perovskites, ACS Nano **10**, 6933 (2016).

[32] J. M. Frost, K. T. Butler, and A. Walsh, Molecular ferroelectric contributions to anomalous hysteresis in hybrid perovskite solar cells, APL Mater. **2**, 081506 (2014).

[33] E. J. Juarez-Perez, R. S. Sanchez, L. Badia, G. Garcia-Belmonte, Y. S. Kang, I. Mora-Sero, and J. Bisquert, Photoinduced giant dielectric constant in lead halide perovskite solar cells, J. Phys. Chem. Lett. **5**, 2390 (2014).

[34] E. T. Hoke, D. J. Slotcavage, E. R. Dohner, A. R. Bowring, H. I. Karunadasa, and M. D. McGehee, Reversible photo-induced trap formation in mixed-halide hybrid perovskites for photovoltaics, Chem. Sci. **6**, 613 (2015).

[35] N. H. Makani, A. Sahoo, P. Pal, T. Paul, L. S. Tanwar, M. Singh, A. Ghosh, and R. Banerjee, Onset of vacancy-mediated high activation energy leads to large ionic conductivity in two-dimensional layered $Cs_2PbI_2Cl_2$ Ruddlesden-Popper halide perovskite, Phys. Rev. Mater. **6**, 115002 (2022).

[36] M. M. Lee, J. Teuscher, T. Miyasaka, T. N. Murakami, and H. J. Snaith, Efficient hybrid solar cells based on meso-superstructured organometal halide perovskites, Science **338**, 643 (2012).

[37] T. Paul, S. Maiti, B. K. Chatterjee, P. Bairi, B. K. Das, S. Thakur, and K. K. Chattopadhyay, Electrochemical performance of 3D network $CsPbBr_3$ perovskite anodes for Li-ion batteries: Experimental venture with theoretical expedition, J. Phys. Chem. C **125**, 16892 (2021).

[38] A. Sahoo, T. Paul, S. Maiti, and R. Banerjee, Temperature-dependent dielectric properties of $CsPb_2Br_5$: A 2D inorganic halide perovskite, Nanotechnology **33**, 195703 (2022).

[39] S. Ahmad, C. George, D. J. Beesley, J. J. Baumberg, and M. De Volder, Photo-rechargeable organo-halide perovskite batteries, Nano Lett. **18**, 1856 (2018).

[40] P. Pal and A. Ghosh, Ionic conduction and relaxation mechanisms in three-dimensional $CsPbCl_3$ perovskite, J. Appl. Phys. **129**, 234102 (2021).

[41] P. Pal and A. Ghosh, Three-dimensional $CsPbCl_3$ perovskite anode for quasi-solid-state Li-ion and dual-ion batteries: Mechanism of Li^+ conversion process in perovskite, Phys. Rev. Appl. **14**, 064010 (2020).

[42] P. Pal and A. Ghosh, Dynamics and relaxation of charge carriers in poly(methylmethacrylate)-based polymer electrolytes embedded with ionic liquid, Phys. Rev. E **92**, 062603 (2015).

[43] S. Mandal and A. Ghosh, Electrical conduction in lead - iron glasses, J. Phys.: Condens. Matter **8**, 829 (1996).

[44] M. Singh, T. Paul, P. Pal, A. Sahoo, L. S. Tanwar, N. H. Makani, A. Ghosh, and R. Banerjee, High ionic conduction and polarity-induced piezoresponse in layered bimetallic $Rb_4Ag_2BiBr_9$ single crystals, J. Phys. Chem. C **126**, 21810 (2022).

[45] See Supplemental Material at http://link.aps.org/supplemental/10.1103/PhysRevApplied.20.054032 for synthesis of the perovskite, details of material characterization, electron density map, energy dispersive optical dielectric function, Debye temperature, heat capacity, enthalpy, and free energy versus temperature, dielectric relaxation time versus reciprocal temperature, stretched exponent, scaling of ac conductivity spectra, details of the calculation of energy and power density, group theory calculation, linear plot of Z' versus $\omega^{-0.5}$.

[46] S. J. Clark, M. D. Segall, C. J. Pickard, P. J. Hasnip, M. I. J. Probert, K. Refson, and M. C. Payne, First principles methods using CASTEP, Zeitschrift für Kristallographie-Crystalline Materials **220**, 567 (2005).

[47] M. D. Segall, J. D. L. Philip, M. J. Probert, C. J. Pickard, P. J. Hasnip, S. J. Clark, and M. C. Payne, First-principles simulation: Ideas, illustrations and the CASTEP code, J. Phys.: Condens. Matter **14**, 2717 (2002).

[48] A. D. Becke, Perspective: Fifty years of density-functional theory in chemical physics, J. Chem. Phys. **140**, 18A301 (2014).

[49] J. P. Perdew, K. Burke, and M. Ernzerhof, Generalized gradient approximation made simple, Phys. Rev. Lett. **77**, 3865 (1996).

[50] A. H. MacDonald, W. E. Picket, and D. D. Koelling, A linearised relativistic augmented-plane-wave method utilising approximate pure spin basis functions, J. Phys. C: Solid State Phys. **13**, 2675 (1980).

[51] W. Zhu, G. Xin, Y. Wang, X. Min, T. Yao, W. Xu, M. Fang, S. Shi, J. Shi, and J. Lian, Tunable optical properties and stability of lead free all inorganic perovskites ($Cs_2SnI_xCl_{6-x}$), J. Mater. Chem. A **6**, 2577 (2018).

[52] B. Saparov, J.-P. Sun, W. Meng, Z. Xiao, H.-S. Duan, O. Gunawan, D. Shin, I. G. Hill, Y. Yan, and D. B. Mitzi, Thin-film deposition and characterization of a Sn-deficient perovskite derivative Cs_2SnI_6, Chem. Mater. **28**, 2315 (2016).

[53] R. Luo, S. Zhang, S. Zhao, J. Li, F. Kang, K. Yu, and G. Wei, Ultrasmall blueshift of near-infrared fluorescence in phase-stable Cs_2SnI_6 thin films, Phys. Rev. Appl. **14**, 014048 (2020).

[54] Z. Xiao, H. Lei, X. Zhang, Y. Zhou, H. Hosono, and T. Kamiya, Ligand-hole in $[SnI_6]$ unit and origin of band gap in photovoltaic perovskite variant Cs_2SnI_6, Bull. Chem. Soc. Jpn. **88**, 1250 (2015).

[55] J. Zhang, C. Yang, Y. Liao, S. Li, P. Yang, Y. Xi, W. Liu, D. A. Golosov, S. M. Zavadski, and S. N. Melnikov, Effect of Li^{+} doping on photoelectric properties of double perovskite Cs_2SnI_6: First principles calculation and experimental investigation, Nanomaterials **12**, 2279 (2022).

[56] U.-G. Jong, C.-J. Yu, Y.-H. Kye, S.-H. Choe, J.-S. Kim, and Y.-G. Choe, Anharmonic phonons and phase transitions in the vacancy-ordered double perovskite Cs_2SnI_6 from first-principles predictions, Phys. Rev. B **99**, 184105 (2019).

[57] J. Liu, C.-g. Duan, W. N. Mei, R. W. Smith, and J. R. Hardy, Dielectric properties and Maxwell-Wagner relaxation of compounds $ACu_3Ti_4O_{12}$ $(A = Ca, Bi_{2/3}, Y_{2/3}, La_{2/3})$, J. Appl. Phys. **98**, 093703 (2005).

[58] M. E. Hajlaoui, R. Dhahri, N. Hnainia, A. Benchaabane, E. Dhahri, and K. Khirouni, Conductivity and giant permittivity study of $Zn_{0.5}Ni_{0.5}Fe_2O_4$ spinel ferrite as a function of frequency and temperature, RSC Adv. **9**, 32395 (2019).

[59] D. K. Pradhan, P. Misra, V. S. Puli, S. Sahoo, D. K. Pradhan, and R. S. Katiyar, Studies on structural, dielectric, and transport properties of $Ni_{0.65}Zn_{0.35}Fe_2O_4$, J. Appl. Phys. **115**, 243904 (2014).

[60] X. Zheng, S. Wang, J. Wang, W. Hua, J. Zhang, and L. Liu, Long-range and short-range transport dynamics of Li ions in $LiMn_2O_4$, J. Phys. Chem. C **124**, 25254 (2020).

[61] A. K. Jonscher, The 'universal' dielectric response, Nature **267**, 673 (1977).

[62] D. P. Almond and A. R. West, Anomalous conductivity prefactors in fast ion conductors, Nature **306**, 456 (1983).

[63] C. G. Koops, On the dispersion of resistivity and dielectric constant of some semiconductors at audiofrequencies, Phys. Rev. **83**, 121 (1951).

[64] K. S. Cole and R. H. Cole, Dispersion and absorption in dielectrics I. Alternating current characteristics, J. Chem. Phys. **9**, 341 (1941).

[65] R. Bergman, General susceptibility functions for relaxations in disordered systems, J. Appl. Phys. **88**, 1356 (2000).

[66] A. Ghosh and A. Pan, Scaling of the conductivity spectra in ionic glasses: Dependence on the structure, Phys. Rev. Lett. **84**, 2188 (2000).

[67] K. Sardar, S. Thakur, S. Maiti, N. Besra, P. Bairi, K. Chanda, G. Majumdar, and K. K. Chattopadhyay, Amalgamation of $MnWO_4$ nanorods with amorphous carbon nanotubes for highly stabilized energy efficient supercapacitor electrodes, Dalton Trans. **50**, 5327 (2021).

[68] R. B. Pujari, V. C. Lokhande, U. M. Patil, D. W. Lee, and C. D. Lokhande, Controlled sulfurization of $MnCO_3$ microcubes architectured MnS_2 nanoparticles with 1.7 fold capacitance increment for high energy density supercapacitor, Electrochim. Acta **301**, 366 (2019).

[69] X. Chen, C. He, W. Wang, T. Bai, G. Xue, and M. Ye, Electrochemical charge storage behavior of various $NiCo_2S_4$ hierarchical microstructures, Phys. Rev. Appl. **15**, 064042 (2021).

[70] A. Noori, M. F. El-Kady, M. S. Rahmanifar, R. B. Kaner, and M. F. Mousavi, Towards establishing standard performance metrics for batteries, supercapacitors and beyond, Chem. Soc. Rev. **48**, 1272 (2019).

[71] Y. Cui, X. Zhao, and R. Guo, Improved electrochemical performance of $La_{0.7}Sr_{0.3}MnO_3$ and carbon co-coated $LiFePO_4$ synthesized by freeze-drying process, Electrochim. Acta **55**, 922 (2010).

[72] A. Izadi-Najafabadi, D. N. Futaba, S. Iijima, and K. Hata, Ion diffusion and electrochemical capacitance in aligned and packed single-walled carbon nanotubes, J. Am. Chem. Soc. **132**, 18017 (2010).

[73] A. Slonopas, H. Ryan, and P. Norris, Ultrahigh energy density $CH_3NH_3PbI_3$ perovskite based supercapacitor with fast discharge, Electrochim. Acta **307**, 334 (2019).

[74] P. Maji, A. Ray, P. Sadhukhan, A. Roy, and S. Das, Fabrication of symmetric supercapacitor using cesium lead iodide ($CsPbI_3$) microwire, Mater. Lett. **227**, 268 (2018).

[75] C. H. Ng, H. N. Lim, S. Hayase, Z. Zainal, S. Shafie, H. W. Lee, and N. M. Huang, Cesium lead halide inorganic-based perovskite-sensitized solar cell for photo-supercapacitor application under high humidity condition, ACS Appl. Energy Mater. **1**, 692 (2018).

[76] S. Thakur, T. Paul, S. Maiti, and K. K. Chattopadhyay, All-inorganic $CsPbBr_3$ perovskite as potential electrode material for symmetric supercapacitor, Solid State Sci. **122**, 106769 (2021).

[77] R. Kumar, P. S. Shukla, G. D. Varma, and M. Bag, Synthesis of porous electrode from $CH_3NH_3PbBr_3$ single crystal for efficient supercapacitor application: Role of morphology on the charge storage and stability, Electrochim. Acta **398**, 139344 (2021).

[78] I. Popoola, M. Gondal, L. Oloore, A. Popoola, and J. AlGhamdi, Fabrication of organometallic halide perovskite electrochemical supercapacitors utilizing quasi-solid-state electrolytes for energy storage devices, Electrochim. Acta **332**, 135536 (2020).

[79] R. Kumar and M. Bag, Quantifying capacitive and diffusion-controlled charge storage from 3D bulk to 2D layered halide perovskite-based porous electrodes for efficient supercapacitor applications, J. Phys. Chem. C **125**, 16946 (2021).

[80] J. K. Pious, M. L. Lekshmi, C. Muthu, R. B. Rakhi, and C. Vijayakumar, Zero-dimensional methylammonium bismuth iodide-based lead-free perovskite capacitor, ACS Omega **2**, 5798 (2017).

[81] T. Li, J. Mallows, K. Adams, G. S. Nichol, J. H. J. Thijssen, and N. Robertson, Thiourea bismuth iodide: Crystal structure, characterization and high performance as an electrode material for supercapacitors, Batteries Supercaps **2**, 568 (2019).

[82] S. Zhou, L. Li, H. Yu, J. Chen, C.-P. Wong, and N. Zhao, Thin film electrochemical capacitors based on organolead triiodide perovskite, Adv. Electron. Mater. **2**, 1600114 (2016).

[83] I. K. Popoola, M. A. Gondal, A. Popoola, and L. E. Oloore, Bismuth-based organometallic-halide perovskite photo-supercapacitor utilizing novel polymer gel electrolyte for hybrid energy harvesting and storage applications, J. Energy Storage **53**, 105167 (2022).

[84] K. Adams, J. Mallows, T. Li, D. Kampouris, J. H. J. Thijssen, and N. Robertson, $Cs_3Bi_2I_9$ as high-performance electrode material achieving high capacitance and stability in an economical supercapacitor, J. Phys. Energy **1**, 034001 (2019).

[85] S. Beniwal, A. Kumar, R. Kumar, A. Suhail, and M. Bag, Tuning conductivity of lead-free $Cs_2AgBiBr_6$ double perovskite ternary composite with PEDOT:PSS and carbon black for supercapacitor application, J. Phys. Chem. C **127**, 12874 (2023).

[86] A. K. Tomar, G. Singh, and R. K. Sharma, Fabrication of a Mo-doped strontium cobaltite perovskite hybrid supercapacitor cell with high energy density and excellent cycling life, ChemSusChem **11**, 4123 (2018).

[87] Y. Liu, Z. Wang, J.-P. M. Veder, Z. Xu, Y. Zhong, W. Zhou, M. O. Tade, S. Wang, and Z. Shao, Highly defective layered double perovskite oxide for efficient energy storage via reversible pseudocapacitive oxygen-anion intercalation, Adv. Energy Mater. **8**, 1702604 (2018).

[88] S. Thakur, S. Maiti, K. Sardar, N. Besra, P. Bairi, K. Panigrahi, K. Chanda, T. Paul, and K. K. Chattopadhyay, new class of trimetallic oxide hierarchical mesoporous array on woven fabric: Electrode for high-performance and stable battery type ultracapacitor, J. Energy Storage **35**, 102249 (2021).

[89] G. Zhang, J. Zhang, Y. Liao, Z. Pan, H. Rao, and X. Zhong, Cs_2SnI_6 nanocrystals enhancing hole extraction for efficient carbon-based $CsPbI_2Br$ perovskite solar cells, Chem. Eng. J. **440**, 135710 (2022).

[90] B. Lee, C. C. Stoumpos, N. Zhou, F. Hao, C. Malliakas, C.-Y. Yeh, T. J. Marks, M. G. Kanatzidis, and R. P. H. Chang, Air-stable molecular semiconducting iodosalts for solar cell applications: Cs_2SnI_6 as a hole conductor, J. Am. Chem. Soc. **136**, 15379 (2014).

[91] L. Zhang, J. Miao, J. Li, and Q. Li, Halide perovskite materials for energy storage applications, Adv. Funct. Mater. **30**, 2003653 (2020).

[92] M. Lathika Divya, Y.-S. Lee, and V. Aravindan, Carbothermally synthesized MoO_2 as an insertion host for high-performance Li-ion capacitors, Phys. Rev. Appl. **19**, 034016 (2023).

[93] R. Kumar, A. Kumar, P. S. Shukla, G. D. Varma, D. Venkataraman, and M. Bag, Photorechargeable hybrid halide perovskite supercapacitors, ACS Appl. Mater. Interfaces **14**, 35592 (2022).